

An emerging and enigmatic spectral class of isolated DAe white dwarfs

Abigail K. Elms,^{1*} Pier-Emmanuel Tremblay,¹ Boris T. Gänsicke,¹ Andrew Swan,¹ Carl Melis,² Antoine Bédard,¹ Christopher J. Manser,³ James Munday,^{1,4} J. J. Hermes,⁵ Erik Dennihy,⁶ Atsuko Nitta,⁷ and Ben Zuckerman⁸

¹*Department of Physics, University of Warwick, Coventry, CV4 7AL, UK*

²*Center for Astrophysics and Space Sciences, University of California, San Diego, CA 92093-0424, USA*

³*Astrophysics Group, Department of Physics, Imperial College London, Prince Consort Rd, London, SW7 2AZ, UK*

⁴*Isaac Newton Group of Telescopes, Apartado de Correos 368, E-38700 Santa Cruz de La Palma, Spain*

⁵*Department of Astronomy, Boston University, 725 Commonwealth Ave., Boston, MA 02215, USA*

⁶*Rubin Observatory Project Office, 950 N. Cherry Ave., Tucson, AZ 85719, USA*

⁷*Gemini Observatory, 670 N A'ohoku Pl., Hilo, Hawaii, HI 96720, USA*

⁸*Department of Physics and Astronomy, University of California, Los Angeles, CA 90095-1562, USA*

Accepted 2023 July 17. Received 2023 July 17; in original form 2023 June 16

ABSTRACT

Two recently discovered white dwarfs, WD J041246.84+754942.26 and WD J165335.21–100116.33, exhibit H α and H β Balmer line emission similar to stars in the emerging DAHe class, yet intriguingly have not been found to have detectable magnetic fields. These white dwarfs are assigned the spectral type DAe. We present detailed follow-up of the two known DAe stars using new time-domain spectroscopic observations and analysis of the latest photometric time-series data from *TESS* and ZTF. We measure the upper magnetic field strength limit of both stars as $B < 0.05$ MG. The DAe white dwarfs exhibit photometric and spectroscopic variability, where in the case of WD J041246.84+754942.26 the strength of the H α and H β emission cores varies in anti-phase with its photometric variability over the spin period, which is the same phase relationship seen in DAHe stars. The DAe white dwarfs closely cluster in one region of the *Gaia* Hertzsprung–Russell diagram together with the DAHe stars. We discuss current theories on non-magnetic and magnetic mechanisms which could explain the characteristics observed in DAe white dwarfs, but additional data are required to unambiguously determine the origin of these stars.

Key words: white dwarfs – stars: interiors – stars: individual (WD J041246.84+754942.26; WD J165335.21–100116.33) – methods: observational – methods: data analysis

1 INTRODUCTION

Almost four decades ago, the isolated white dwarf GD 356 (WD 1639+537) was discovered and found to be magnetic with a hydrogen-dominated atmosphere and Zeeman-split H α and H β Balmer line emission triplets (Greenstein & McCarthy 1985). It was assigned the spectral class DAHe, a degenerate (D) star with Balmer lines (A), Zeeman-splitting (H) and emission (e). GD 356 was later found to be photometrically variable over a period of 115 minutes (Brinkworth et al. 2004; Wickramasinghe et al. 2010). GD 356 remained the only member of its class until a few years ago, when Gänsicke et al. (2020) and Reding et al. (2020) discovered two new DAHe stars. These new stars evidenced spectroscopic variability in the H α and H β emission features in addition to photometric variability. Walters et al. (2021) conducted recent work on GD 356 with new time-resolved data and also confirmed spectroscopic and photometric variability in this white dwarf. Survey data and targeted spectroscopic follow-up of DAHe candidates, selected due to their photometric variability from hundreds of thousands of white dwarf

candidates first identified from the spacecraft *Gaia* (Gaia Collaboration et al. 2023), have led to the discovery of 26 DAHe stars to date (Manser et al. 2023; Reding et al. 2023).

Two interesting white dwarfs, WD J041246.84+754942.26 (hereafter WD J0412+7549; Tremblay et al. 2020) and WD J165335.21–100116.33 (hereafter WD J1653–1001; O’Brien et al. 2023), have emerged over the past few years and been classified as DAe – they have hydrogen-dominated atmospheres and exhibit weaker H α and H β line emission than DAHe stars, but intriguingly lack an observable magnetic field i.e. do not show Zeeman-split emission line triplets. These two stars, in addition to two of the 26 DAHe white dwarfs, lie within 40 pc of the sun. There are 1066 white dwarfs in the 40 pc volume-limited sample of white dwarfs (McCleery et al. 2020; O’Brien et al. 2023) of which 655 are classified as DA, so the identification of four DA white dwarfs with Balmer emission lines to date within this volume attests to a fraction of 0.61 per cent. The two DAe and 26 DAHe stars closely cluster in one region on the *Gaia* Hertzsprung–Russell diagram (HRD; Gänsicke et al. 2020; Walters et al. 2021; Manser et al. 2023) and have a remarkable homogeneity in atmospheric parameters, with effective temperatures $7400 \text{ K} \lesssim T_{\text{eff}} \lesssim 8500 \text{ K}$ and white dwarf

* Contact e-mail: Abigail.Elms@warwick.ac.uk

masses $0.5 M_{\odot} \lesssim M_{\text{WD}} \lesssim 0.8 M_{\odot}$. The DAe and DAHe stars with reliable time-resolved data have measured variability periods of $\approx 0.08 - 36$ h, which is plausibly linked to the rotation period.

DAe and DAHe white dwarfs are encapsulated into one DA(H)e class in this work based on our initial hypothesis that these objects have a similar origin but differ in terms of magnetic field strength and possibly other properties. The magnetic field strengths observed at the surface of DAHe stars range from $\approx 5 - 147$ MG (Greenstein & McCarthy 1985; Gänsicke et al. 2020; Reding et al. 2020; Walters et al. 2021; Manser et al. 2023; Reding et al. 2023), resulting in a range of physical effects acting upon the white dwarfs including altered or suppressed surface convection and possibly altered hydrostatic structure of atmospheric layers (Landstreet 1987; Tremblay et al. 2015; Ferrario et al. 2015; Fuller & Mathis 2023). However, $86 \pm 7_{10}$ per cent of magnetic white dwarfs within the same region of the *Gaia* HRD do not show Balmer line emission (Manser et al. 2023), suggesting that magnetic field strength is not the only physical parameter defining the DA(H)e class. Recent analyses of DA(H)e stars show no evidence of binarity or ongoing accretion of planetary debris (e.g. see Tremblay et al. 2020, for the DAe WD J0412+7549). Note that there are instances of DAe+dM systems in the literature where the Balmer emission is related to binarity (e.g. Silvestri et al. 2006, 2007; Gianninas et al. 2011), but these systems are not discussed in this work.

Previous studies have explored intrinsic (e.g. stellar structure and internal dynamics) and extrinsic (e.g. planetary mass companions and binary interactions) mechanisms to explain the observations of DA(H)e white dwarfs (Gänsicke et al. 2020; Reding et al. 2020; Schreiber et al. 2021b; Walters et al. 2021; Ginzburg et al. 2022; Reding et al. 2023). An active chromosphere which is hosted by a (magnetic) dark surface spot/region is one explanation for Balmer emission lines. The close clustering of DA(H)e objects on the *Gaia* HRD could be explained by a convective dynamo driven by white dwarf core crystallization occurring at a specific time in the cooling sequence (Gänsicke et al. 2020; Ginzburg et al. 2022), although this scenario has recently been questioned (Fuentes et al. 2023). While no DA(H)e star to date has been found in a binary system, it has been suggested that Balmer line emission could be caused by a planetary mass companion, possibly from magnetic induction in a close-in orbit (Goldreich & Lynden-Bell 1969; Li et al. 1998; Wickramasinghe et al. 2010). However, no study has been able to unambiguously conclude on a suitable scenario therefore the mechanism(s) causing emission in DA(H)e white dwarfs remains a mystery.

In this work, we present new time-domain spectroscopic observations of the two DAe stars, WD J0412+7549 and WD J1653–1001, and analyse their time-series observations from the Transiting Exoplanet Survey Satellite (*TESS*; Ricker et al. 2014) and Zwicky Transient Facility (ZTF; Bellm et al. 2019; Masci et al. 2019). In Section 2, we present photometric and spectroscopic time-domain observations of WD J0412+7549 and WD J1653–1001. We analyse the data of both white dwarfs in Section 3 to obtain atmospheric parameters, investigate photometric and spectroscopic line variability and determine limits on radial velocity shifts. In Section 4, we discuss our results and conclude in Section 5.

2 OBSERVATIONS AND DATA

2.1 Broad-band photometry

WD J0412+7549 and WD J1653–1001 have photometry in the optical from *Gaia* DR3 and the Panoramic Survey Telescope and Rapid

Table 1. Optical and IR photometry, including magnitudes from different filters, for WD J0412+7549 and WD J1653–1001.

Survey	Filter	WD J0412+7549 [mag]	WD J1653–1001 [mag]
<i>Gaia</i>	<i>G</i>	15.815 ± 0.003	15.708 ± 0.003
	<i>G_{BP}</i>	15.922 ± 0.004	15.851 ± 0.005
	<i>G_{RP}</i>	15.626 ± 0.005	15.385 ± 0.007
Pan-STARRS	<i>g</i>	15.916 ± 0.008	15.872 ± 0.005
	<i>r</i>	15.900 ± 0.004	15.736 ± 0.004
	<i>i</i>	15.948 ± 0.003	15.766 ± 0.001
	<i>z</i>	16.047 ± 0.004	15.817 ± 0.002
	<i>y</i>	16.124 ± 0.005	15.886 ± 0.008
2MASS	<i>J</i>	15.544 ± 0.064	15.122 ± 0.057
	<i>H</i>	15.412 ± 0.133	15.064 ± 0.086
	<i>K</i>	15.519 ± 0.235	15.076 ± 0.138

Response System (Pan-STARRS; Chambers et al. 2016; Flewelling et al. 2020) DR2, in addition to near-IR photometry from the Two Micron All Sky Survey (2MASS; Skrutskie et al. 2006). Table 1 displays the available photometric data. We do not include photometry from the Wide-field Infrared Survey Explorer (*WISE*; Wright et al. 2010) CatWISE2020 catalogue (Marocco et al. 2021) in photometric fits for either object performed in this work as the close proximity of background sources results in the contamination of *WISE* measurements. WD J0412+7549 is ≈ 15 arcsec away from the edge-on dusty galaxy LEDA 2769388 (Paturel et al. 2003) which has an estimated redshift of $z = 0.07$ (Dályá et al. 2018). WD J1653–1001 is ≈ 1 arcsec away from a background main-sequence star (Gaia DR3 4334641562479650816).

Stellar parameters – including spectral type, astrometry and atmospheric parameters – for WD J0412+7549 and WD J1653–1001 are shown in Table 2. Details on the photometric and spectroscopic fits performed to calculate the atmospheric parameters are given in Section 3.2.

2.2 Time-domain spectroscopy

Spectroscopic observations of WD J0412+7549 were made using four different ground-based telescopes spanning 27 months. The long time-frame between observations allows for a dedicated search for variability in the Balmer emission lines. Observational details are listed in Table 3 for WD J0412+7549 and WD J1653–1001, including the exposure times (t_{exp}), number of exposures (n_{exp}) and the total duration of each observing run. Sections 2.2.1 – 2.2.4 discuss the observations of WD J0412+7549 made with each telescope in detail. Section 2.2.5 presents the spectroscopic observations of WD J1653–1001.

2.2.1 WHT/ISIS

Intermediate-resolution spectroscopy of WD J0412+7549 was obtained with the double-arm Intermediate-dispersion Spectrograph and Imaging System (ISIS) on the Cassegrain focus of the 4.2-m William Herschel Telescope (WHT) at the Observatorio del Roque de los Muchachos on La Palma, Spain. We used the default CCD detectors EEV12 2048×4096 pixel² in the blue (R600B grating, resolving power $R \approx 2000$) arm and RED+ 2048×4096 pixel² in the red (R600R grating, $R \approx 2700$) arm. The approximate wavelength ranges covered by the blue and red arms in our observations are 3100 – 5400 Å and 5700 – 9000 Å, respectively, thus all Balmer line ($H\alpha$ to $H\zeta$) regions were observed. We used a slit width of 1.2 arcsec

Table 2. Observed and derived parameters of WD J0412+7549 and WD J1653–1001. Atmospheric parameters were calculated by performing photometric (Phot) and weighted 3D spectroscopic (3D spec; see text for details) fits. Values are given in the J2016.0 epoch.

Parameter		WD J0412+7549	WD J1653–1001	
Designation		<i>Gaia</i> DR3 551153263105246208	<i>Gaia</i> DR3 4334641562477923712	
Spectral type		D Ae	D Ae	
RA		04:12:46.23	16:53:35.21	
Dec		+75:49:42.68	–10:01:16.33	
Parallax	ϖ [mas]	28.53 ± 0.03	30.65 ± 0.04	
Distance	d [pc]	35.05 ± 0.04	32.63 ± 0.04	
Proper motion	μ_α [mas yr ^{–1}]	-140.90 ± 0.03	159.38 ± 0.05	
	μ_δ [mas yr ^{–1}]	26.11 ± 0.03	-211.01 ± 0.03	
Absolute magnitude	M_G [mag]	13.092 ± 0.003	13.140 ± 0.003	
Effective temperature	T_{eff} [K]	8546 ± 87	7388 ± 71	(Phot)
		8578 ± 106	7613 ± 95	(3D spec)
Surface gravity	$\log g$ [cm s ^{–2}]	8.260 ± 0.030	7.930 ± 0.030	(Phot)
		8.316 ± 0.025	7.893 ± 0.030	(3D spec)
Mass	M_{WD} [M_\odot]	0.76 ± 0.02	0.55 ± 0.02	(Phot)
		0.80 ± 0.02	0.53 ± 0.02	(3D spec)
Radius	R [$\times 10^{-5} R_\odot$]	1072 ± 19	1331 ± 23	(Phot)
		1027 ± 19	1366 ± 26	(3D spec)
Cooling age	τ [Gyr]	1.290 ± 0.057	1.154 ± 0.048	(Phot)
		1.419 ± 0.086	1.019 ± 0.050	(3D spec)
Magnetic field strength	B [MG]	< 0.05	< 0.05	
Spin period	P [h]	2.2891144 ± 0.0000016	80.534 ± 0.087	

Table 3. Time-domain spectroscopic observations for WD J0412+7549 and WD J1653–1001 obtained from ground-based telescopes, detailing the exposure time (t_{exp}), number of exposures (n_{exp}) for each observing run and the duration of the observing run. Numbers separated by a colon represent exposures taken in the blue:red arms.

Object	Date	Telescope/Instrument	t_{exp} (s)	n_{exp}	Duration (h)
WD J0412+7549	2018-Oct-14	WHT/ISIS	600	3	0.56
	2018-Oct-15	WHT/ISIS	600	1	0.17
	2018-Oct-16	WHT/ISIS	600	1	0.17
	2019-Dec-09	Keck/HIRES	1800	2	4.29
	2020-Aug-17	INT/IDS	1200	2	0.67
	2020-Aug-18	INT/IDS	900	12	3.14
	2020-Oct-04	Gemini/GMOS-N	300	8	0.73
	2020-Oct-05	Gemini/GMOS-N	300	8	0.73
	2021-Jan-12	Gemini/GMOS-N	300	20	2.08
WD J1653–1001	2018-May-22	Shane/KAST	3000:1000	1:3	0.83
	2023-May-15	Shane/KAST	2000:1000	2:4	1.11

and dispersions of 0.49 Å/pixel in the blue arm and 0.45 Å/pixel in the red arm. We imposed a binning of 2×2 , resulting in an average resolution of ≈ 2 Å.

Observations were taken on 2018 October 14–16 with 600 s exposures. Three exposures were taken on 2018 October 14 while one exposure was taken on each of the subsequent nights.

2.2.2 Keck/HIRES

High-resolution optical spectra of WD J0412+7549 were obtained on 2019 December 9 from the High Resolution Echelle Spectrometer (HIRES; Vogt et al. 1994) instrument on the Keck-1 10-m telescope at the W. M. Keck Observatory, Hawaii. Observations were taken using the mosaic of three MIT-Lincoln Lab (MIT/LL) 2000×4000 pixel² CCDs with the red collimator (HIRESr) and C5 decker ($R \approx 40\,000$), with slit width 1.148 arcsec and 1×2 binning. The wavelength coverage of our HIRES observations is approximately 4800 – 6700 Å, with small gaps between echelle orders. The H α and H β line regions were covered with this setup with an average resolution of ≈ 0.15 Å.

Two 1800 s exposures were taken of WD J0412+7549 with 3.79 h

separation (time between exposure start times) as a check for emission line variability. The spectra were reduced and extracted using the HIRES software package MAKEE¹. Keck observed the standard star Feige 110 on the same night as WD J0412+7549 so we used this spectrum to correct for the instrumental response function (IRF) of the telescope. Although Feige 110 has H α and H β lines, the rest of the spectrum is featureless and an accurate representation of the IRF. Therefore, we used 1 – 3 orders before/after the Balmer line regions in Feige 110 to correct the spectra of WD J0412+7549.

2.2.3 INT/IDS

We collected intermediate-resolution spectroscopic observations of WD J0412+7549 on two consecutive nights using the Intermediate Dispersion Spectrograph (IDS) on the Cassegrain focus of the 2.5-m Isaac Newton Telescope (INT), located at the Observatorio del Roque de los Muchachos on La Palma, Spain. Our setup utilized the EEV10

¹ <https://sites.astro.caltech.edu/tb/makee/>

4096 × 2048 pixel² CCD detector in the blue arm with a slit width of 1.2 arcsec. We used the R632V grating centred at 5720 Å, resulting in a dispersion of 0.90 Å/pixel over the approximate wavelength range 4200 – 7000 Å with a spectral resolution of $R = 2400$. We employed 1×1 binning and have an average resolution of ≈ 2 Å.

Two 1200 s exposures were taken on 2020 August 17 and twelve 900 s exposures were taken on 2020 August 18. Spectroscopic coverage was achieved for Balmer lines from $H\alpha$ to $H\gamma$.

2.2.4 Gemini/GMOS-N

We used the Gemini Multi-Object Spectrograph (GMOS; Hook et al. 2004) instrument on the 8-m Gemini-North Telescope (Gemini-N/GMOS-N) to search for variability in the Balmer line emission of WD J0412+7549 over multiple epochs as part of programme GN-2020B-Q-304. Long-slit spectroscopic observations were performed using the three GMOS-N 2048 × 4176 pixel² Hamamatsu CCD (Scharwächter et al. 2018) chips. The B600+G5307 grating ($R \approx 1700$) was used with a central wavelength of 5300 Å and 2×2 binning. The approximate wavelength range covered by our observations is 3900 – 6700 Å. Our setup resulted in a dispersion of 0.45 Å/pixel and an average resolution of ≈ 3 Å.

Eight consecutive 300 s exposures were taken on 2020 October 4 and 5, with an additional observation taken on 2021 January 12 that consisted of 20 consecutive 300 s exposures. The spectra were flux calibrated and cover Balmer lines from $H\alpha$ to $H\delta$. The additional $H\epsilon$ Balmer line is also covered by the 2021 January 12 observing run.

2.2.5 Shane/KAST

We observed WD J1653–1001 using the KAST Double Spectrograph on the Shane 3-m Telescope at the Lick Observatory in California, USA. We utilized the default set-up of the KAST spectrograph, using a Fairchild 2000 × 2000 pixel² CCD in the blue arm and a Hamamatsu 2000 × 4000 pixel² CCD in the red arm. We observed with a D57 dichroic and a 600/4310 grism for the blue side and a 830/8460 grating for the red side, with respective dispersions of 0.43 Å/pixel and 1.02 Å/pixel. The approximate wavelength range covered by the blue arm was 3600 – 5300 Å and by the red arm was 5700 – 7800 Å. We used a slit width of 1 arcsec, which achieved a resolution of ≈ 1 Å in the blue arm and ≈ 2 Å in the red arm.

The first observation took place on 2018 May 22, with one 3000 s exposure taken in the blue arm and three consecutive 1000 s exposures taken in the red arm. The second observation was taken on 2023 May 15, with two consecutive 2000 s exposures taken in the blue arm and four consecutive 1000 s exposures taken in the red arm. Spectroscopic coverage was achieved for all Balmer lines from $H\alpha$ to $H\zeta$.

2.3 TESS observations of WD J0412+7549

The *TESS* spacecraft observed WD J0412+7549 under designation TIC 103222871 in Sectors 19, 25 and 26 during Cycle 2, Sectors 52 and 53 in Cycle 4, and Sector 59 in Cycle 5. Observations were taken between 2019 November 28 and 2022 December 23 (see Table 4). Exposure times of 120 s were taken in all six sectors. WD J0412+7549 has a *TESS* magnitude of $T \approx 15.7$.

Pre-search Data Conditioning Simple Aperture Photometry (PDC-SAP) light curves were used for our analysis in Section 3.1.1 as these have systematic errors removed, including error sources from the telescope and the spacecraft (Stumpe et al. 2012; Smith et al. 2012). The

PDCSAP light curves for WD J0412+7549 were retrieved from the Mikulski Archive for Space Telescopes (MAST) public data portal. We used the *tsa* context within MIDAS² to carry out the time-series analysis of the *TESS* data.

2.4 ZTF observations of WD J1653–1001

ZTF is a robotic time-domain survey which uses the 48-inch Schmidt Telescope at the Palomar Observatory in California, USA (Masci et al. 2019). In this work, we use DR15 observations of WD J1653–1001 which were taken in the green- (*g*) and red- (*r*) bands of ZTF between 2018 March 17 and 2022 November 09. The light curves were retrieved from the public NASA/IPAC Infrared Science Archive (IRSA). Exposure times of 30 s were taken in all observations.

3 ANALYSIS

3.1 Photometric and spectroscopic variability

All spectroscopic analysis of WD J0412+7549 in this work was performed on the IRF corrected Keck data and flux calibrated Gemini, INT and WHT data. All observation time-stamps for WD J0412+7549 and WD J1653–1001 were converted to a Barycentric Julian Date (BJD) Barycentric Dynamical Time (TDB). The time format used for all data is Barycentric Modified Julian Date (BMJD) minus 50 000 which is BJD(TDB) – 2 450 000.5.

3.1.1 Photometric variability of WD J0412+7549

Walters et al. (2021) analyzed a single sector of *TESS* data of WD J0412+7549 and identified photometric variability with a period of 2.28910 ± 0.00002 h. Here, we computed discrete Fourier transforms individually for all six sectors of *TESS* data obtained so far (see Section 2.3). All power spectra contained a single, strong signal at a period of ≈ 2.29 h. We determined the spin period and its uncertainty by performing a sine-fit to the data using $\Delta\text{flux} = A\sin(2\pi t/P - \phi) + c$ in each sector, where A is the amplitude, t is the observation time of each measurement, P is the period, ϕ is the phase-shift and c is an offset. The results are reported in Table 4. The *TESS* ephemeris closest to the centre of the entire dataset which corresponds to the photometric maximum is $\text{BMJD} - 50\,000 = 9368.75658(31) + 0.095379756(93)E$, so we chose this as an epoch T_0 to phase all *TESS* light curves to the same baseline.

Further, we computed a discrete Fourier transform of the entire *TESS* observations (Figure 1). No other strong peaks were detected across the periodogram and the period at ≈ 2.29 h is detected above a false alarm probability (FAP) of one per cent. The inset of Figure 1 shows the power spectrum around the confirmed period, and displays a complex alias pattern which is consistent with the window function due to the sparse sampling across the full baseline spanned by the *TESS* data.

A magnetic field can result in inhomogeneous brightness distributions across the white dwarf surface, which in turn leads to photometric variability on the white dwarf spin period (e.g. Brinkworth et al. 2013). The combined data from the six *TESS* sector observations clearly show the photometric variability of WD J0412+7549

² MIDAS is available from the European Southern Observatory

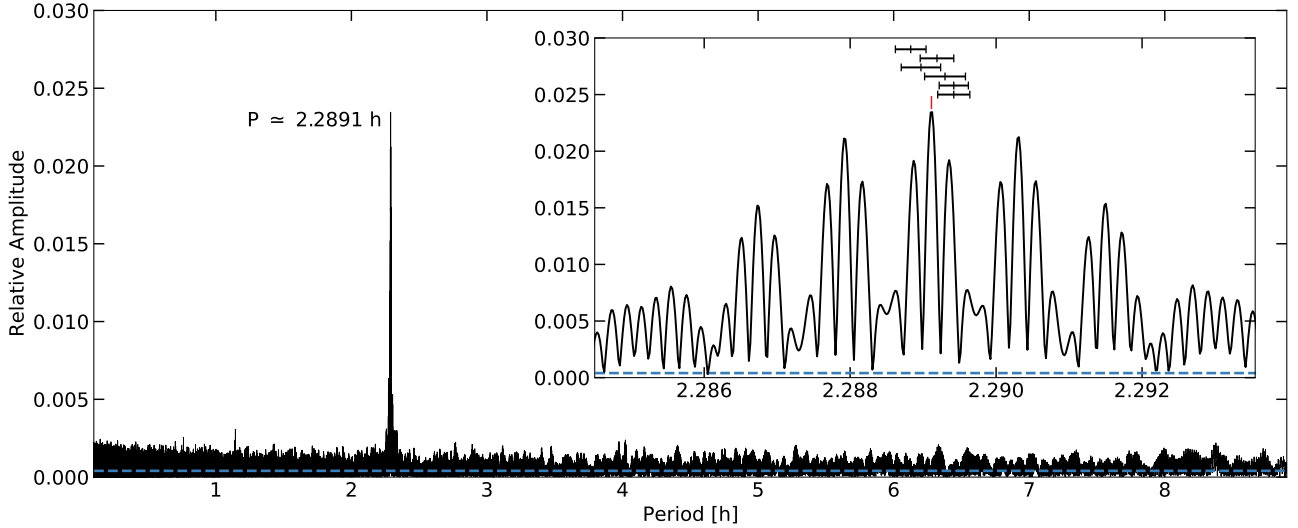


Figure 1. Power spectrum computed from the combined *TESS* observations of WD J0412+7549. The strongest periodic signal is at $P \approx 2.2891$ h and is detected above a FAP of one per cent (blue dashed line). Inset is a zoom-in on the strongest signal, where the red tick above the central signal represents the uncertainty of the period determined from a sine fit to the combined *TESS* data and the six black error bars illustrate the periods and uncertainties derived from the six individual *TESS* sectors (see Table 4).

Table 4. Dates of the six *TESS* observations of WD J0412+7549 and white dwarf spin periods measured from sine-fits to each sector independently. A combined period was measured from combining all sectors and fitting a sine function. Amplitudes from the sine-fits are reported here.

Sector	Dates	Period [h]	Amplitude [per cent]
19	2019 Nov 28 – Dec 23	2.28942(22)	2.69 ± 0.13
25	2020 May 13 – Jun 08	2.28942(20)	2.68 ± 0.12
26	2020 Jun 08 – Jul 04	2.28930(28)	2.23 ± 0.13
52	2022 May 18 – Jun 13	2.28897(27)	2.05 ± 0.12
53	2022 Jun 13 – Jul 09	2.28919(23)	2.16 ± 0.11
59	2022 Nov 26 – Dec 23	2.28883(21)	2.22 ± 0.10
Combined		2.2891144(16)	2.29 ± 0.05

(Figure 2). The top panel of Figure 2 shows the light curve consisting of all data points folded upon the best-fitting period, in addition to the same data binned into 400 phase bins. A sinusoidal shape is visible when the light curve is extended over two phases. The bottom panel of Figure 2 shows the zoomed-in light curve on the 400 phase bins with a fitted sinusoid overlaid in red. The period obtained from a sine fit to the combined *TESS* data is 2.2891144(16) h. The period uncertainty is much smaller than the separation between the three central aliases in the power spectrum, and we hence conclude that this is an unambiguous measurement of the spin period of the white dwarf throughout the *TESS* observations – under the assumption that the period is constant.

We investigated the possibility that the period measured for WD J0412+7549 is actually half the period of variability, due to there being potentially two poles or emission spots (Manser et al. 2023; Reding et al. 2023). We inspected the phase-folded light curves on both $P = 2.2891144(16)$ h and $2P$, but no additional structures were evident on twice the period. Therefore, we assume the periodic signal detected is likely the spin-period of the white dwarf assuming a single emission spot.

Inspecting the *TESS* spin measurements (Table 4) may suggest a trend of a decrease with time. The reduced χ^2 of the periods measured from the six *TESS* sectors against the assumption of a

constant period is ≈ 1.5 , which hints that the period may not be constant. However, an observed minus calculated ($O - C$) analysis does not evidence a significant period change, as the line of best-fit gradient is -0.007 ± 0.061 with a reduced $\chi^2 \approx 1.03$. We also performed an F -test to determine the significance of a linear trend to the full set of data, testing the null-hypothesis that a linear trend is not reflective of the data presented. Following the methodology described in Munday et al. (2023), we find an F -ratio of 20.53 which, under the $F(1, n - 2)$ distribution for our $n = 6$ measurements, indicates that there is a 98.94 per cent (2.6σ) significance of a linear trend in the data. We note that the apparent decreasing trend in the individual periods may be related to small phase or period drifts, or simply be an artifact of the instrument. For now, we caution against over-interpreting the apparent trend and recommend that the spin period of WD J0412+7549 should keep being monitored.

In the bottom panel of Figure 2, the phase coverage of each exposure taken with the WHT, Keck, INT and Gemini telescopes are represented with horizontal coloured bars. WD J0412+7549 was observed on three consecutive nights with the WHT, which covered ≈ 31 per cent of the periodic signal identified. The two 30-minute exposures taken by Keck resulted in ≈ 44 per cent of the spin period being spectroscopically covered. The INT exposures taken over two consecutive nights covered ≈ 98 per cent of the spin period. The Gemini exposures taken in 2021 covered ≈ 79 per cent of the spin period, but together with the 2020 exposures ≈ 87 per cent was covered. Considering all of the above observations, we have achieved full spectroscopic phase coverage of WD J0412+7549 with short-cadence observations which allowed us to analyse the emission line variability over the entire spin period (Section 3.1.3).

3.1.2 Photometric variability of WD J1653–1001

The g -band and r -band flux of WD J1653–1001 was calculated from the ZTF magnitude data, relative to the median magnitude in each band. We combined the g -band and r -band datasets and weighted the contribution of the individual band points equally. Then, we computed Lomb-Scargle periodograms (Lomb 1976; Scargle 1982)

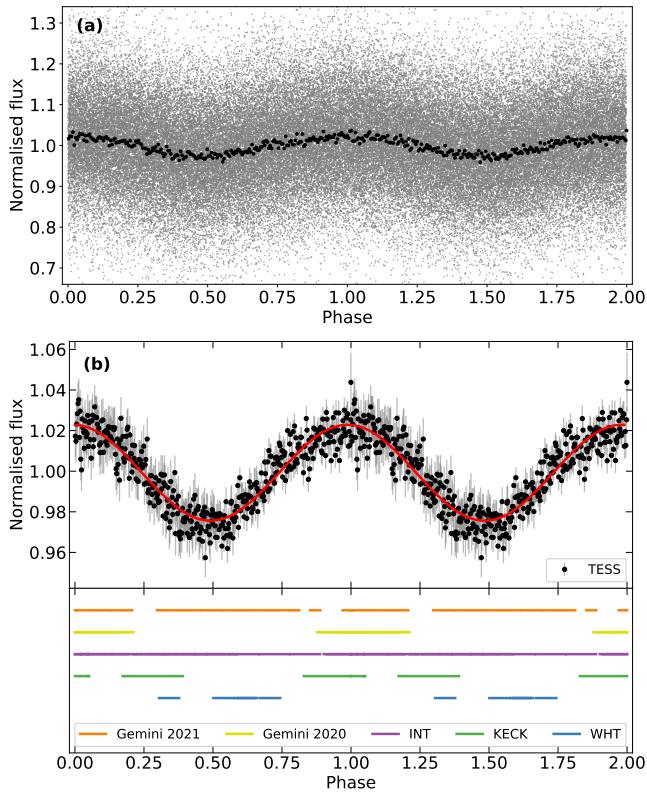


Figure 2. The combined *TESS* data from the individual 120 s cadence observations of WD J0412+7549 showing (a) all data points (grey) folded at the best-fitting period and the same data binned into 400 data points (black), and (b) the binned data points (black) fitted with a sine wave (red overlay) at the same period as the light curve and the phase of the spectroscopic observations. Full spectroscopic phase coverage by the WHT (blue), Keck (green), INT (purple) and Gemini telescopes is achieved. Gemini observations taken in 2020 (yellow) and 2021 (orange) are distinguished. The data in all panels are repeated over two phases for illustrative purposes. Phase = 0 corresponds to the photometric maximum at $T_{\text{BMD}} - 50,000 = 9368.75658(31)$ d. Error bars are not shown in (a) for clarity but are shown in (b) to represent the 1σ scatter in each bin.

using the `python` package `astropy.timeseries` (Astropy Collaboration et al. 2013, 2018, 2022) for the individual *g*-band and *r*-band light curves in addition to the combined *g*- and *r*-band light curve (Figure 3).

The strongest signals in all three power spectra occur at periods ≥ 11.5 h. ZTF is sensitive to shorter periods than *TESS* due to shorter exposure times, so if WD J1653–1001 had a similar period with similar amplitude to that found for WD J0412+7549 then it would be detected. The strongest signal in the *g*-band power spectrum is at a period of ≈ 29.4729644 h which we attribute to the moon and not as a true measurement of the white dwarf spin period.

Out of the five strongest signals in all three power spectra, only the periodic signal at ≈ 80.31 h is common to all three and is detected above a FAP of one per cent³. The period of ≈ 80.31 h is the strongest signal in the combined *g*- and *r*-band power spectrum, the second strongest signal in the *r*-band power spectrum and the third strongest signal in the *g*-band power spectrum. However, with the current ZTF

data it is not possible to unambiguously determine whether the peaks at ≈ 80.31 h are aliases related to the sampling rate or are indeed the intrinsic periodic signal. We note that the periodic signal at ≈ 18.48 h is the strongest signal in the *r*-band and second strongest signal in the combined *g*- and *r*-band power spectra, however it is the 23rd strongest signal in the *g*-band power spectrum, so is not considered the dominant periodic signal at this time.

Despite the uncertainty related to the period, we created phase-folded light curves on a 80.31 h period with the *g*-band, *r*-band and combined *g*- and *r*-band data and fit them with a sinusoidal function. There is very little variation between the *g*-band and *r*-band light curves (Figure 4), with the amplitudes of both differing by $< 1\sigma$. Therefore, we used the combined *g*- and *r*-band light curve to measure the period of WD J1653–1001 from the sine fit, which resulted in 80.534 ± 0.087 h and an amplitude 2.3 ± 0.2 per cent. The period uncertainty is within 1σ of the strongest detected periodic signal and is much smaller than the separation between adjacent aliases in the power spectrum. Previous studies from Reding et al. (2020) and Manser et al. (2023) found a colour dependence on the strength of variability in DAHe stars, so WD J1653–1001 differs from DAHe stars in this way as no colour dependence is evident.

We performed further analysis to determine the likelihood that the measured periodic signal of 80.534 ± 0.087 h is intrinsic to WD J1653–1001, due there being a background main-sequence star ≈ 1 arcsec away from this white dwarf. The proper motion of WD J1653–1001 reveals that over the span of ZTF observations included in DR15, the white dwarf moved from one side of the main-sequence star to the other while almost directly passing in-front of it. There is no indication that WD J1653–1001 and the contaminant were resolved into separate sources by ZTF so we cannot exclusively determine with ZTF whether the period of variability is sourced from WD J1653–1001 or the contaminant.

To help determine whether the periodic signal is coming from WD J1653–1001 or the contaminant, we created a variability metric to investigate the likelihood of the objects being variable. Our variability metric takes a similar approach to Guidry et al. (2021), which was used by Reding et al. (2023) to identify the DAHe stars LP 705–64 and WD J143019.29–562358.33. Our metric compensates for some systematic effects and is easy to interpret: it returns a sigma value relative to the median photometric scatter of sources of similar brightness and sky position. For example, the two stars just mentioned return 3.9σ and 5.5σ , respectively, i.e. they show significantly more photometric scatter than similar sources.

The variability metric is calculated using the scatter in individual *Gaia* *G*-band observations. That quantity is not directly available, so it is estimated for every source in the catalogue as $S = \sqrt{\text{PHOT_G_N_OBS}/\text{PHOT_G_MEAN_FLUX_OVER_ERROR}}$. The distribution of S for sources of the same brightness should be approximately Gaussian, with a long tail of high values for variable sources. To model that distribution across the catalogue, the 16th, 50th, and 84th quantiles of S (denoted e.g. S_{50}) are determined within many magnitude bins. The local distribution of S for any given source can then be estimated by interpolation. The variability of that source is then calculated as $\sigma_S = (S - S_{50})/S_{16}$ where $S < S_{50}$, or $\sigma_S = (S - S_{50})/S_{84}$ where $S > S_{50}$. However, inspection of σ_S values across the sky of such values reveals the clear imprint of the *Gaia* scanning law. Fractional residuals S/S_{50} are calculated for every source in the catalogue, and the median of those residuals calculated within every level-7 HEALpix pixel. Those positional medians provide a correctional scaling factor, as the median residual within each HEALpix pixel should be unity in the absence of systematics. The scaling factor is interpolated between HEALpix pixel

³ The modulation in the *g*- and *r*-band are near identical so the FAP of the combined datasets is a very good approximation.

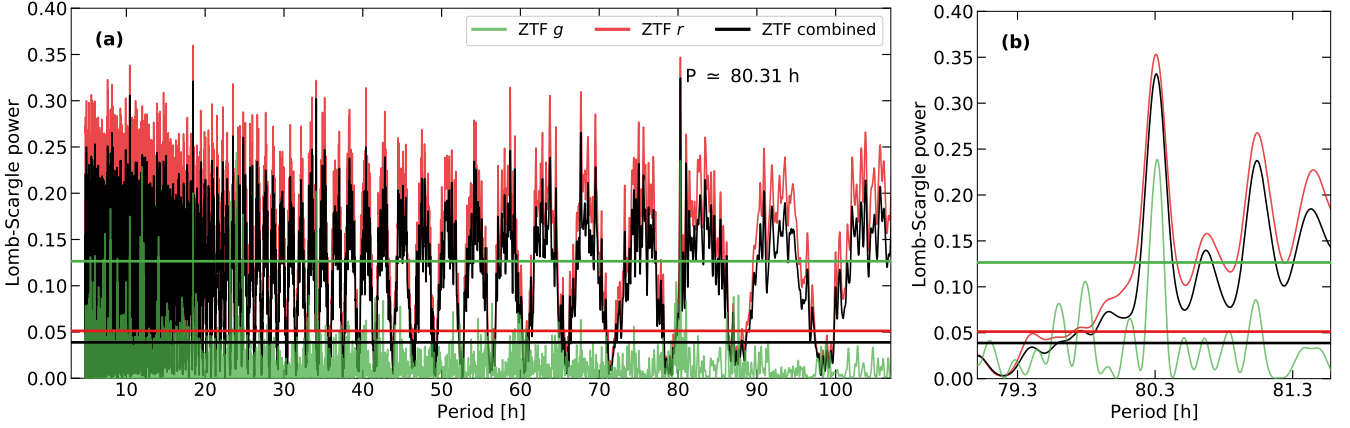


Figure 3. Power spectra computed from the *g*-band, *r*-band and combined *g*- and *r*-band DR15 ZTF data of WD J1653–1001. The signal common to all power spectra out of the five strongest signals in the individual power spectra corresponds to a period of ≈ 80.31 h, which is detected above a FAP of one per cent (green, red and black solid lines). Panel (b) shows the power spectra zoomed in on the periodic signal at ≈ 80.31 h. The legend applies to both panels.

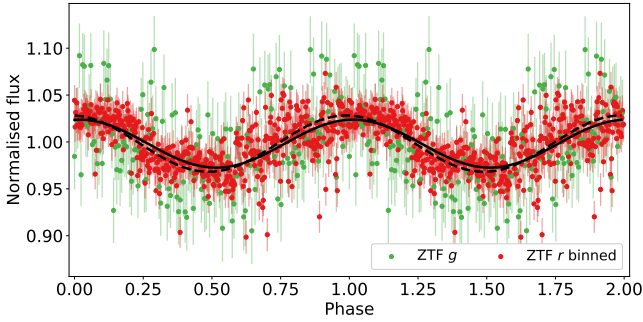


Figure 4. ZTF DR15 *g*- (green) and *r*- (red) band light curves of WD J1653–1001, phase-folded onto a period of 80.31 h. Sine waves were fitted on the *g*- and *r*-band light curves, shown by the black dashed and solid curves, respectively. The *g*-band raw data are shown, whereas the *r*-band data has been binned into 400 data points. The data are repeated over two phases for illustrative purposes. Phase = 0 corresponds to the photometric maximum at $T_{\text{BJMD}-50000} = 9701.44(5)$ d for the *g*-band light curve and $T_{\text{BJMD}-50000} = 9702.07(5)$ d for the *r*-band light curve. Error bars are shown to represent the 1σ scatter in each measurement/bin.

centres and used to correct S across the entire catalogue. Quantiles of S are then recalculated within each magnitude bin, and the whole procedure iterated until the positional corrections converge on unity.

We assessed photometric variability S for both objects compared to a random sample of 10 000 main-sequence stars from the same region of the *Gaia* HRD as the background object. Both WD J1653–1001 and the contaminant are 5σ outliers, meaning either both or one of them is photometrically variable but *Gaia* cannot fully resolve the two objects. Of the 10 000 main-sequence stars, 2.5 per cent are variable at or above 5σ . Using the same variability metric on the sample of DA(H)e stars revealed that the two DAe stars and one DAHe star are variable at or above 5σ . The DAHe stars have a median variability of 0.6σ , with the maximum being 5.5σ . Therefore, 10.7 per cent of DA(H)e stars and 100 per cent of DAe stars are variable above 5σ which are both larger than the probability that the variability is coming from the contaminant main-sequence star.

As a last check, we looked in *Gaia* DR3 which has entries for WD J1653–1001 and the contaminant and found the `phot_variable_flag` parameter (Eyer et al. 2017, 2023) identi-

fied variability in the photometric data for WD J1653–1001, but unfortunately the photometric data of the main-sequence star was not processed or exported to the catalogue. The four DA(H)e stars which have a median photometric error above 3.9σ are classified as variable in *Gaia* DR3 which provides validation to our own variability metric.

The possibility of WD J1653–1001 having surface features more complex than a single spot/region beneath the chromosphere cannot be ruled out with the current ZTF data. The phase-folded light curve on $2P = 161.068$ h has two maxima and minima per cycle which could suggest the presence of two emission spots/regions (Manser et al. 2023; Reding et al. 2023). If this is the case, then the period of variability would be $2P$, with the measured period of 80.534 ± 0.087 h being an alias. However, we cannot confidently conclude either way due to the uncertainty surrounding the ZTF periodic signal analysis.

The combination of the ZTF power spectra, phase-folded light curve, *Gaia* DR3 variability flag and our own variability check makes us confident that WD J1653–1001 is photometrically variable, with a dominant periodic signal of 80.534 ± 0.087 h. However, only by obtaining full phase coverage of this star with dedicated follow-up time-domain observations – which has ideally been resolved for WD J1653–1001 and the contaminant main-sequence star – will it be possible to unambiguously confirm whether the measured periodic signal is the true spin period for WD J1653–1001, if it is an alias, or if it is indeed the period of variability for the contaminant.

3.1.3 Spectroscopic variability

Spectra taken of WD J0412+7549 using the WHT (Figure A1), Keck (Figure 5), INT (Figure A2) and Gemini (Figure A3) telescopes all evidence H α and H β line emission. The emission line strength clearly changes between exposures taken over the spin period, which is strong evidence of emission line variability.

WD J0412+7549 was observed by the WHT on three consecutive nights. Multiple observations were made on the first night so the stacked spectrum is presented in Figure A1, in addition to the single spectra taken on the subsequent two nights. Erroneous wavelength shifts were apparent in the original spectra suggesting that improper wavelength calibration had been performed. A reliable wavelength calibration could not be performed on these spectra, hence we do not pursue this avenue further.

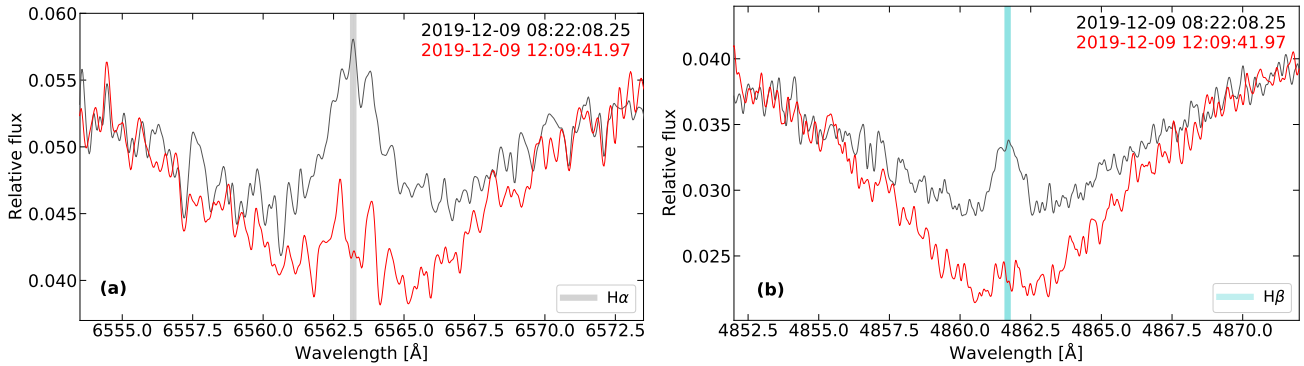


Figure 5. Two 30-minute exposures of WD J0412+7549 taken with the Keck HIRES instrument. Spectra were taken 3.79 h apart around the emission core of (a) $H\alpha$ and (b) $H\beta$. The coloured vertical bars indicate the rest wavelengths of $H\alpha$ (grey) and $H\beta$ (aqua) corrected for radial velocity (Section 3.3). All spectra have had the instrumental response function removed (see text for details) and are smoothed with a 5-pixel boxcar for clarity. The observation UT date and start times are shown in the top right corner of the plots.

Two 30-minute exposures covering the $H\alpha$ and $H\beta$ line regions were taken with Keck of WD J0412+7549 and are shown in Figure 5. It is clear that both Balmer emission lines change in strength between exposures, which were taken 227.56 min apart. Broad emission wings are evident in both exposures, and likely result from the different temperature and pressure stratifications of the atmosphere and chromosphere in (possibly magnetic) spots. However, further investigation is required to confirm this.

The $H\alpha$ and $H\beta$ emission line variability is seen in all exposures of the INT (Figure A2) and Gemini (Figure A3) observations, where the line strength variation is observed more gradually due to shorter exposures taken almost over the entire spin period (Figure 2). Only the $H\alpha$ and $H\beta$ line regions are shown in Figure A2 as the $H\gamma$ line region is cut off by the INT flux calibration and is therefore not reliable. Out of the observations performed with the Gemini telescope, the $H\alpha$ and $H\beta$ emission line variability is most clearly seen in the exposures taken on 2021 January 12 therefore we only show these spectra in Figure A3. Almost pure atmospheric $H\alpha$ emission and absorption features are visible in the exposures taken at 07:27:29 and 08:26:58, respectively, which occur nearly half a spin period apart (0.433 phase difference).

The spectra of WD J1653–1001 taken with the KAST instrument on 2018 May 22 and 2023 May 15 are shown in Figure 6, which consists of the individual exposure taken in the blue arm on 2018 May 22 and the stacked spectra from the other exposures. Coverage of the $H\alpha$ to $H\zeta$ line regions was achieved, where the emission cores of $H\alpha$ to $H\beta$ are clearly visible.

None of the Balmer emission lines in WD J0412+7549 nor WD J1653–1001 spectra exhibit Zeeman-splitting therefore no magnetic field detection or strength measurements could be made. Instead, we measured the upper limit of the magnetic field strength using the first Keck exposure of WD J0412+7549, as it has the highest resolution out of all the observations, and the first KAST spectrum of WD J1653–1001. We constructed a delta function and convolved it with the spectral resolution of the instrument. We then Zeeman-split the delta function, overlaid it on the $H\alpha$ emission core and altered the magnetic field strength until the delta function was wide enough that we would visually see Zeeman-splitting and be able to distinguish it from the noise. This technique yielded upper limits on the magnetic field strength $B < 0.05$ MG for both DAe stars. The magnetic field limit obtained from Keck is limited by the intrinsic widths of emission features and the length of the exposures (0.219 of the phase). We cannot exclude the possibility of spin-related magnetic smearing

in the emission core over the exposure, or intrinsic broadening from a high temperature chromosphere. Hence, we obtain a similar magnetic field limit from Keck and KAST for both white dwarfs, despite the difference in instrumental resolution.

To investigate the emission activity of WD J0412+7549, we measured the equivalent widths (W_λ) of the $H\alpha$ and $H\beta$ emission cores in all exposures, where the smaller the value of W_λ corresponds to stronger emission. The W_λ were normalized using the python package `scikit-learn` (Pedregosa et al. 2011) with an L2 normalization, then compared against the phase of each exposure. On average, the W_λ uncertainties are larger for $H\beta$ emission cores which are noisier and shallower than the $H\alpha$ emission cores. Figure 7 displays the W_λ of the $H\alpha$ and $H\beta$ emission line cores as a function of phase, where $\phi = 0$ corresponds to the photometric maximum at $T_{\text{BJD}} - 50\,000 = 9368.75658(31)$ d. The data are repeated over two phases for clarity. We fitted a sinusoid to the data to clearly show that the weakest emission (i.e. largest W_λ) occurs at $\phi = 0$. In contrast, Figure 2 shows that the photometric flux maximum occurs at $\phi = 0$. Hence, there is an anti-phase relationship between the photometric and emission line variability of WD J0412+7549.

The same analysis of W_λ against phase could not be performed for WD J1653–1001 as there is not enough time-resolved spectroscopic data for this star. However, we measured the W_λ of the $H\alpha$ emission feature in the three KAST exposures taken in the red arm on 2018 May 22, and found that all three have an identical W_λ . The lack of spectral variability over the 3000 s baseline would be consistent with a large period, possibly with the one found by ZTF (Section 3.1.2), and the spectra taken on 2023 May 15 (Figure 6) confirms variability over a longer baseline.

3.2 Photometric and spectroscopic parameters

Photometric and spectroscopic fits were performed to calculate the atmospheric parameters of WD J0412+7549 and WD J1653–1001. The best-fitting model for DAe stars was ascertained by testing three DA model atmospheres: 1D radiative, 1D convective and 3D convective (Tremblay et al. 2013, 2015).

The photometric fits of WD J0412+7549 and WD J1653–1001 were performed using photometry from *Gaia* DR3, Pan-STARRS and 2MASS (Table 1). Both DAe stars have ≈ 2.3 per cent flux variability (see Sections 3.1.1 and 3.1.2) so, based on Eq.16 from Gentile Fusillo et al. (2019), we imposed a lower limit of 0.025 mag on the photometric uncertainties from Pan-STARRS and 2MASS.

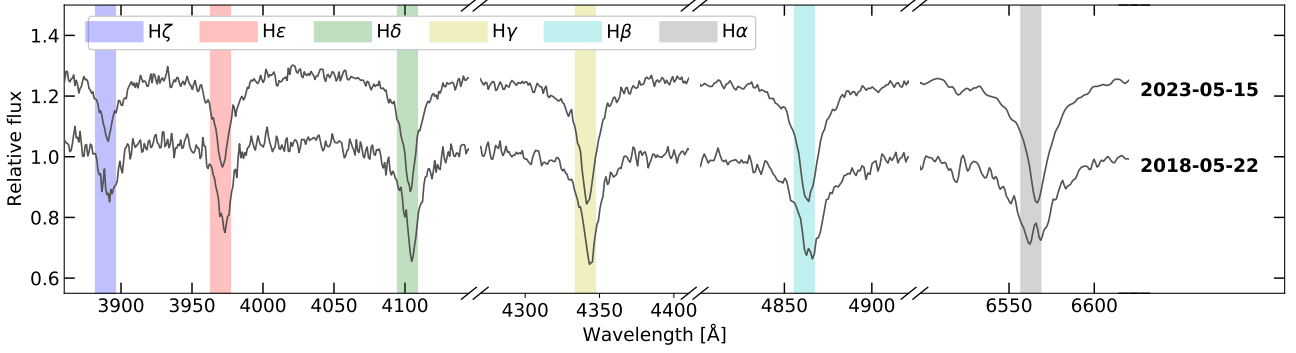


Figure 6. Spectra of WD J1653–1001 taken with the KAST spectrograph on 2018 May 22 and 2023 May 15 around the H α to H ζ Balmer line regions. Shown is the individual spectrum taken in the blue arm on 2018 May 22 and the stacked spectra from the other exposures. The observation UT dates are shown on the right of the plot. Spectra are convolved with a Gaussian with a FWHM of 2 Å and offset vertically for clarity.

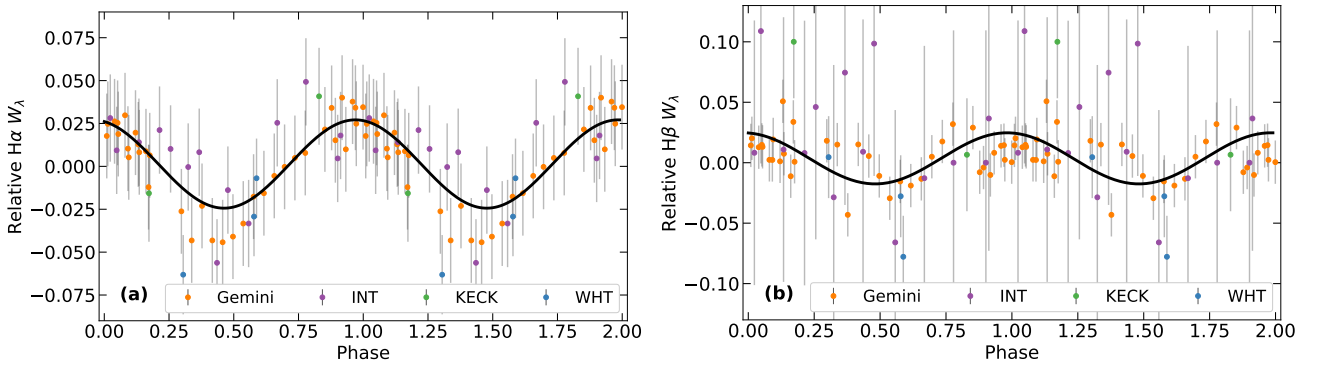


Figure 7. The phase of WD J0412+7549 as a function of the relative equivalent width (W_λ) of its spectroscopically observed (a) H α and (b) H β Balmer lines by the WHT (blue), Keck (green), INT (purple) and Gemini (orange) telescopes. The data are fitted with a sine wave (black overlay) and repeated over two phases for illustrative purposes. Weakest emission corresponds to the largest W_λ , which occurs at $\phi = 0$ (i.e. photometric maximum). Error bars correspond to 1σ uncertainties.

There are 395 and 599 repeat observations of WD J0412+7549 and WD J1653–1001 in *Gaia* DR3, respectively, thus the G , G_{BP} and G_{RP} measurements stated in *Gaia* DR3 are likely averages over each star’s full rotation period which are suitable to use to calculate their photometric parameters. The *Gaia* DR3 measured uncertainties are likely more precise than our imposed lower limit on the Pan-STARRS and 2MASS measurements, therefore we did not modify these uncertainties.

We tested the photometric fits using the three DA model atmospheres however the differences between atmospheric parameters were negligible. The best-fitting atmospheric parameters were found to be $T_{\text{eff}} = 8546 \pm 87$ K and $\log g = 8.260 \pm 0.030$ dex for WD J0412+7549 and $T_{\text{eff}} = 7388 \pm 71$ K and $\log g = 7.930 \pm 0.030$ dex for WD J1653–1001 (Table 2).

Figure 8 shows the spectral energy distribution (SED) created from the photometric fits of WD J0412+7549 and WD J1653–1001 with observed and synthetic photometry. Reasonable fits were achieved between the observed and synthetic photometry for both DAe stars. The bandpasses of the *Gaia* filters are broad therefore arbitrary nominal wavelengths were used for the SED. There is no near-IR excess seen in the SED of either DAe star.

We conducted spectroscopic fits using the three DA model atmospheres (like in our photometric fits) on the WHT spectra of WD J0412+7549 and on the KAST spectra of WD J1653–1001. The continuum was initially fit on each spectrum with free parameters to

extract the Balmer lines. The normalized Balmer lines were then re-fit to give the best-fitting model. We removed H α lines as the emission core made it challenging to accurately fit the spectra. The central regions around the line cores of the other Balmer lines were also removed to achieve the most accurate fit. The WHT observations for WD J0412+7549 and KAST observations for WD J1653–1001 have approximately equivalent S/N so the weighted mean of the corresponding sets of T_{eff} and $\log g$ were taken as the spectroscopic atmospheric parameters for each model. Similar to our photometric fits, we added the corresponding uncertainty from the ≈ 2.3 per cent flux variability of each DAe star to the T_{eff} spectroscopic weighted mean uncertainty. Estimating the uncertainty on the spectroscopic weighted mean of $\log g$ from flux variation is not trivial, so we did not modify those uncertainties.

The 1D convective model provided a worse agreement between photometry and spectroscopy than the more realistic 3D convective model (Tremblay et al. 2013) so was discarded. It has been argued that magnetic fields suppress convective energy transfer in white dwarfs (Tremblay et al. 2015; Bédard et al. 2017; Gentile Fusillo et al. 2018; Gänsicke et al. 2020; Cunningham et al. 2021) in the regime ≥ 0.01 MG at $T_{\text{eff}} \approx 8500$ K, which results in an altered atmospheric temperature structure. Therefore, radiative models are appropriate for stars with $B \geq 0.01$ MG whereas convective models are best suited for stars with lower magnetic field strengths. We measured the maximum magnetic field strength limit of WD J0412+7549 and

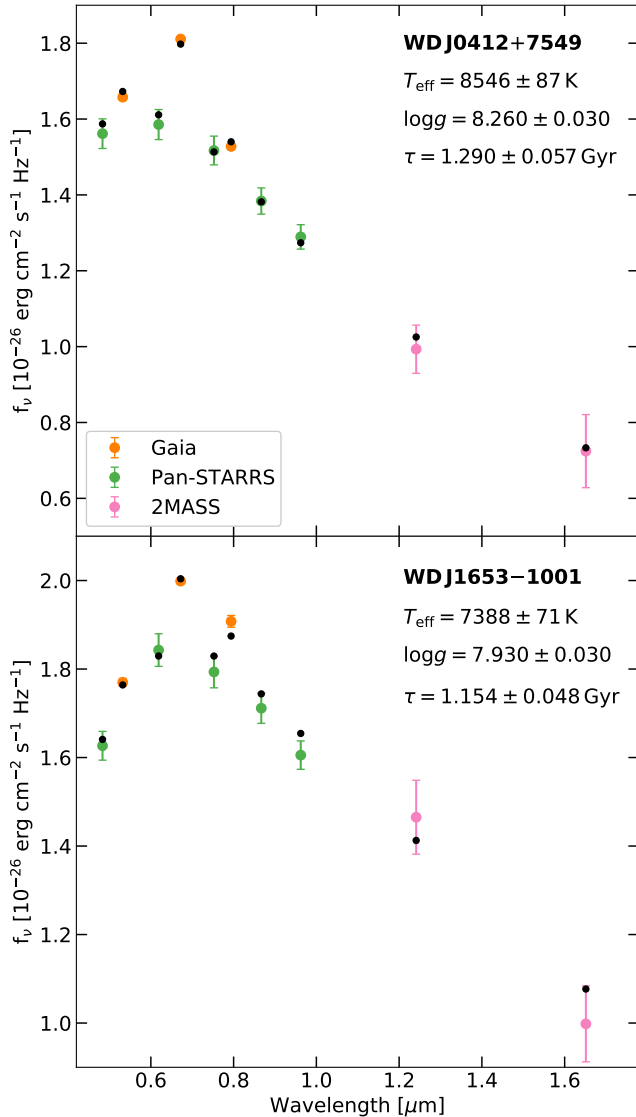


Figure 8. Photometric fits between the observed (coloured) and synthetic (black) photometry for WD J0412+7549 and WD J1653–1001. Uncertainties of the Pan-STARRS and 2MASS measurements have an imposed lower limit of 0.025 mag. Error bars correspond to 1σ uncertainties.

WD J1653–1001 as $B < 0.05$ MG therefore either the 1D radiative or 3D convective model could be valid for these stars.

The 1D radiative spectroscopic fit yielded $T_{\text{eff}} = 8015 \pm 100$ K and $\log g = 8.305 \pm 0.023$ dex for WD J0412+7549 and $T_{\text{eff}} = 6951 \pm 88$ K and $\log g = 7.622 \pm 0.035$ dex for WD J1653–1001. These results are 4σ and 2σ away from the photometric T_{eff} and $\log g$ calculated for WD J0412+7549, and 4σ and 7σ away from the photometric T_{eff} and $\log g$ calculated for WD J1653–1001, respectively.

The 3D convective spectroscopic fit yielded $T_{\text{eff}} = 8578 \pm 106$ K and $\log g = 8.316 \pm 0.025$ dex for WD J0412+7549 and $T_{\text{eff}} = 7613 \pm 95$ K and $\log g = 7.893 \pm 0.030$ dex for WD J1653–1001. These results are 1σ and 2σ away from the photometric T_{eff} and $\log g$ calculated for WD J0412+7549, and 2σ and 1σ away from the photometric T_{eff} and $\log g$ calculated for WD J1653–1001, respectively.

The atmospheric parameters obtained using the 3D convective

model are in better agreement with the photometric parameters for each star, thus we use 3D convective models for our spectroscopic fits and parameters (Table 2). The spectroscopic fits using the 3D convective model for the WHT observations of WD J0412+7549 and KAST observations of WD J1653–1001 are shown in Figure 9, and Figure 10 shows the corresponding T_{eff} and $\log g$ parameters obtained from these fits in addition to the weighted mean of the 3D spectroscopic fit parameters and the parameters obtained from the photometric fits.

The photometric parameters for both DAe stars are likely more accurate than the spectroscopic parameters as they are less sensitive to the convection model or emission core removal procedure. Therefore, we use the atmospheric parameters obtained from the photometric fit as our adopted parameters for WD J0412+7549 and WD J1653–1001.

3.3 Radial velocity of WD J0412+7549

The Balmer emission observed in DAe stars could have intrinsic or extrinsic origins. To test for an extrinsic origin, we searched for evidence of a companion using the radial velocity (v_{rad}) of the $H\alpha$ emission line core from multiple spectroscopic exposures. We measured the wavelength shift of the $H\alpha$ emission line central components in WD J0412+7549 compared to rest wavelengths in all Keck, INT and Gemini spectroscopic data. The spectra observed using Keck are of the highest spectral resolution compared to the other observations so are the most reliable to calculate the radial velocity of WD J0412+7549. A reliable radial velocity variation of WD J1653–1001 cannot be calculated with the available KAST spectra.

Our procedure consisted of creating a Gaussian of a fixed-width and convolving it by the spectral resolution of the instrument at the $H\alpha$ line. We then fitted the Gaussian to the emission line 10 000 times while moving it horizontally within the noise of the core emission wings. The peak of the fitted Gaussian which corresponded to the minimum convolution between the Gaussian and emission line was the best-estimate of the central wavelength of the emission line. The Keck spectroscopic data were reduced with MAKEE and output with vacuum wavelengths corrected to the heliocentric reference frame, but as no further corrections were made we imposed a lower limit of 5 km s^{-1} for radial velocity uncertainties. For consistency, we applied the same lower limit for all radial velocity uncertainties.

The line velocity obtained by the first Keck observation taken at 08:22:08.25 UT was $21.2 \pm 6.5 \text{ km s}^{-1}$. The second Keck observation was taken at 12:09:41:97 UT, which is at a 0.438 phase shift from the end of the first exposure. The $H\alpha$ core emission line variability between exposures is significant, with the second Keck exposure evidencing a much shallower emission core (Figure 5). The $H\alpha$ emission line in the first Keck exposure has an approximate Gaussian structure thus our fitting procedure to measure the line velocities was successful. Accurately measuring the $H\alpha$ line velocity in the second Keck exposure proved challenging because the emission drastically decreases and the S/N ratio does not allow us to confidently say if there is sub-structure within the emission lines. Since the earlier Keck exposure clearly showed the emission line cores to have a Gaussian structure, we assumed the core in the second exposure does too. We therefore performed the same fitting procedure on the second Keck exposure to yield the $H\alpha$ emission line velocity of $14.3 \pm 7.2 \text{ km s}^{-1}$.

The gravitational redshift of WD J0412+7549 was calculated to be $45.1 \pm 1.5 \text{ km s}^{-1}$. Correcting the emission line velocities for the gravitational redshift yielded v_{rad} of $-23.9 \pm 6.6 \text{ km s}^{-1}$ and $-30.7 \pm 7.4 \text{ km s}^{-1}$ for the first and second Keck exposures, respec-

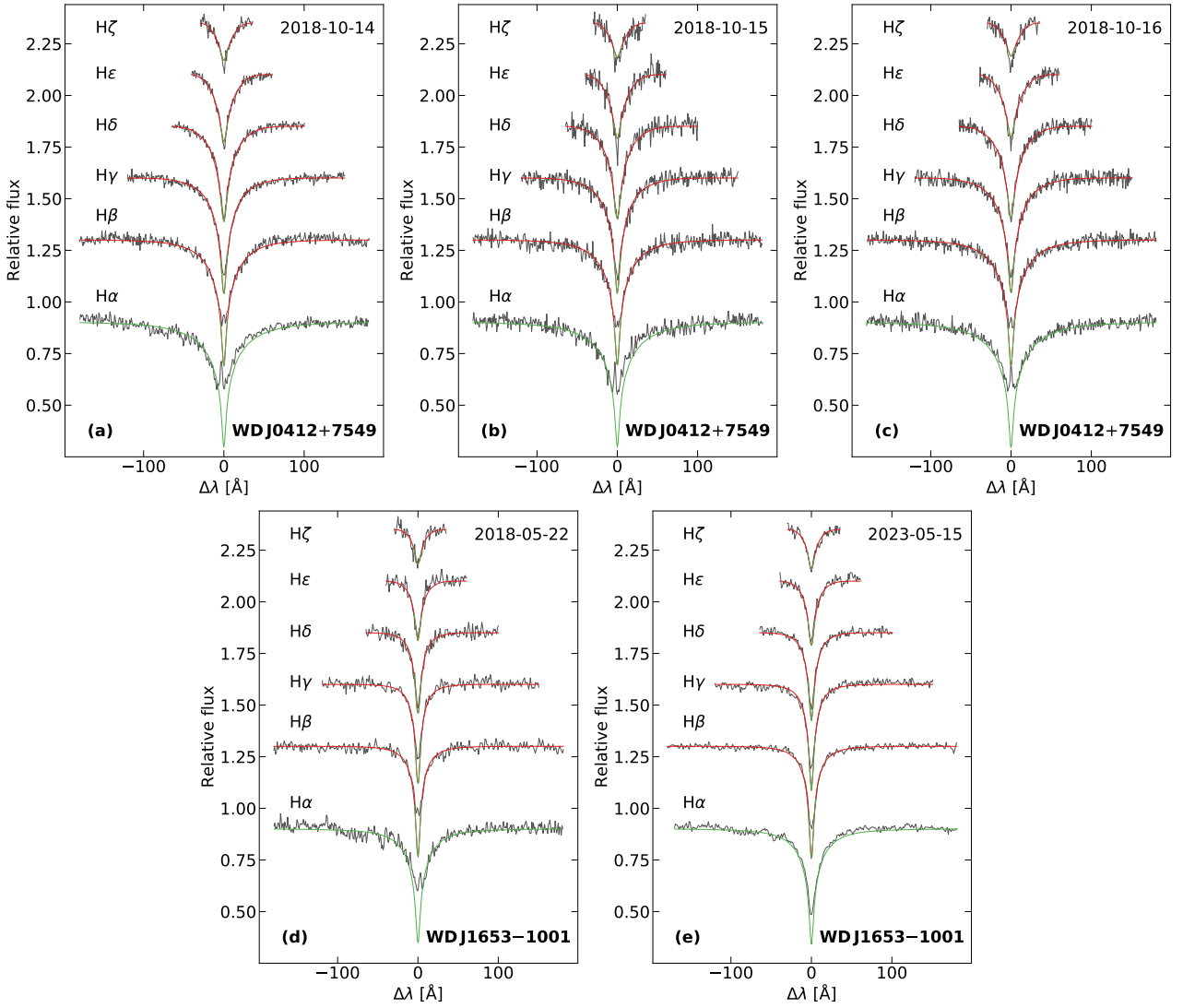


Figure 9. Spectroscopic fits of the normalized observed Balmer line profiles (black) with a 3D convective DA model atmosphere for (a-c) the WHT spectra of WD J0412+7549 and (d-e) the KAST spectra of WD J1653–1001, where the UT date of the observation is in the top right corner of the plots. The best-fitting model is overlaid in red and the green lines are the regions which were removed from the fit. Lines are offset vertically for clarity.

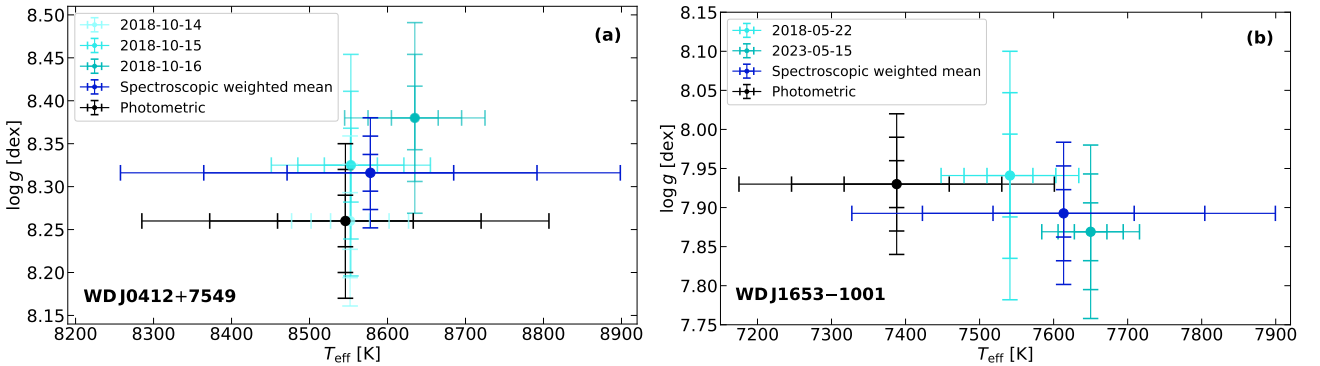


Figure 10. Atmospheric parameters obtained from photometric and 3D spectroscopic fits of (a) WD J0412+7549 and (b) WD J1653–1001. 3D spectroscopic fits were performed on each WHT observation of WD J0412+7549 and KAST observation of WD J1653–1001, with their corresponding T_{eff} and $\log g$ shown in varying shades of light blue. The 3D spectroscopic weighted mean (dark blue) of the parameters calculated from the individual 3D spectroscopic fits are shown, along with the parameters calculated from the photometric fits (black). Error bars correspond to 1σ , 2σ and 3σ uncertainties.

tively. The direction of movement of WD J0412+7549 is unknown so we only consider the radial velocity variation. Therefore, the radial velocity variation of WD J0412+7549 is $6.9 \pm 9.9 \text{ km s}^{-1}$ for a phase difference of 0.438, which is consistent with zero. Using the same fitting procedure on all Gemini spectra, we get an upper limit on the radial velocity variation of $\lesssim 40 \text{ km s}^{-1}$.

3.4 Core crystallization

The onset of crystallization has been suggested as a potential scenario for the close clustering of DA(H)e stars on the *Gaia* HRD (see Section 4.1) and for the production of their magnetic fields through a crystallization-driven convective dynamo (Isern et al. 2017; Schreiber et al. 2021a,b).

We investigated whether the two DAe stars have started crystallizing and, if so, what percentage of their interior is crystallized. To this end, we computed new model evolutionary sequences using the STELUM code (Bédard et al. 2022). Our white dwarf models consist of a carbon/oxygen/ ^{22}Ne core, surrounded by a standard helium mantle ($M_{\text{He}}/M_{\text{WD}} = 10^{-2}$) and a "thick" outermost hydrogen layer ($M_{\text{H}}/M_{\text{WD}} = 10^{-4}$). The core composition is initially uniform, with a standard ^{22}Ne mass fraction of 1.4 per cent. As for the oxygen mass fraction, the appropriate value is still quite uncertain, which is unfortunate given that this parameter significantly affects the crystallization process (i.e. a more oxygen-rich white dwarf starts to crystallize earlier; Fontaine et al. 2001; Bauer et al. 2020). On one hand, current pre-white dwarf evolutionary models typically predict central oxygen abundances between 60 and 70 per cent (Renedo et al. 2010; Salaris et al. 2022; Bauer 2023). However, these predictions are notoriously uncertain due to our poor knowledge of nuclear reaction rates and convective boundary mixing in the core helium burning phase (Straniero et al. 2003; Salaris et al. 2010; De Gerónimo et al. 2019; Giammichele et al. 2022). On the other hand, recent asteroseismological analyses of pulsating white dwarfs hint that the central oxygen abundance may be closer to (and perhaps even higher than) 80 per cent (Giammichele et al. 2018, 2022). To account for this uncertainty, we computed two sets of sequences assuming core oxygen mass fractions of 60 and 80 per cent, respectively.

Our new sequences also incorporate several notable improvements at the level of the input physics with respect to the sequences published in Bédard et al. (2020). We included the energy released by ^{22}Ne diffusion in the liquid phase and by carbon/oxygen phase separation upon crystallization, as outlined in Bédard et al. (2022) and with minor updates discussed in Venner et al. (2023). We also made use of the improved carbon/oxygen phase diagram of Blouin & Dalgault (2021), which is a critical ingredient to accurately model the crystallization process. Finally, we employed the envelope conductive opacities of Blouin et al. (2020), which result in a faster cooling and thus a slightly earlier onset of crystallization with respect to the previous conductive opacities of Cassisi et al. (2007).

Figure 11 shows the predicted crystallized fraction (by mass) for WD J0412+7549 and WD J1653–1001 according to our model evolutionary sequences. Assuming a core oxygen abundance of 60 per cent, crystallization has not started for WD J0412+7549 below 1σ . At 3σ , the crystallized fraction could reach ≈ 15 per cent. However, if we assume a core oxygen abundance of 80 per cent for WD J0412+7549, then the predicted crystallized fraction is ≈ 15 per cent. At 1σ the crystallized fraction could increase to 20 per cent, and further increase to almost 40 per cent at 3σ . Crystallization has not started for WD J1653–1001 up to 3σ when assuming either core oxygen abundances.

4 DISCUSSION

4.1 Physical characteristics of DA(H)e stars

WD J0412+7549 and WD J1653–1001 lack observable Zeeman-split Balmer lines in their emission cores upon inspection of their spectra (see Section 3.1.3), hence have no detectable magnetic field and are classified as DAe. This is an important difference with the larger DAHe class as these stars have Zeeman-split Balmer lines with measured field strengths in the range $\approx 5 - 147 \text{ MG}$ (Greenstein & McCarthy 1985; Gänsicke et al. 2020; Reding et al. 2020; Walters et al. 2021; Manser et al. 2023; Reding et al. 2023), which are 2–3 orders of magnitude higher than the upper limit determined for DAe white dwarfs. There are known magnetic white dwarfs with field strengths between 0.05–5 MG, e.g. in the 40 pc sample (Bagnulo & Landstreet 2021, 2022; O’Brien et al. 2023) so possible reasons for the apparent absence of DA(H)e stars in this field range are: poor spectroscopic phase-coverage of magnetic DA stars resulting in the misclassification of DA(H)e stars as DAH or DA due to phase-dependent emission (Manser et al. 2023); the emission strength may correlate with magnetic field strength, making the identification of Zeeman-split Balmer emission lines more difficult at low magnetic field strengths and in spectra which are not of high S/N or resolution (Bagnulo & Landstreet 2018; Ferrario et al. 2020). Dedicated and high-resolution spectroscopic follow-up of all white dwarfs in the relevant portion of the *Gaia* HRD is required to understand whether this gap of field strengths in DA(H)e white dwarfs is real or a selection effect.

However, DAe stars have undeniable similarities to the larger DAHe class. None of the known DA(H)e stars exhibit metal absorption features in their spectra – even high-resolution spectra of WD J0412+7549 does not show evidence of metal pollution, as predicted in Walters et al. (2021) – which suggests they are not actively accreting nor have recently accreted planetary material (Koester et al. 1997; Jura 2003; Gänsicke et al. 2019). Also, all DA(H)e stars closely cluster in one region of the *Gaia* HRD in $G_{\text{BP}} - G_{\text{RP}}$ versus G_{abs} compared to the parameter space occupied by white dwarf candidates within 100 pc of the sun (Figure 12; Gentile Fusillo et al. 2019). Manser et al. (2023) explored the close clustering of DA(H)e stars and found that within the cluster region ≈ 3 per cent of white dwarfs are classified as DA(H)e and $\approx 10 - 30$ per cent of DAH stars exhibit Balmer line emission. The close clustering could suggest that Balmer line emission is a consequence of a short-lived evolutionary stage of DAH or DA white dwarfs which have cooling ages of $> 1 \text{ Gyr}$ (Manser et al. 2023). The cause of the trigger of Balmer line emission in this niche evolutionary stage is still unknown.

There is a homogeneity in atmospheric parameters of the DA(H)e stars as they have $7400 \text{ K} \lesssim T_{\text{eff}} \lesssim 8500 \text{ K}$ and white dwarf masses $0.5 M_{\odot} \lesssim M_{\text{WD}} \lesssim 0.8 M_{\odot}$. The spin period of WD J0412+7549 is consistent with those of DAHe stars which fall in the range $\approx 0.08 - 36 \text{ h}$. We derived a tentative spin period of $\approx 80.5 \text{ h}$ for WD J1653–1001 (Section 3.1.2) which is slower than the spin periods of other DA(H)e stars. We confirm spectral variability for WD J1653–1001, as we find evidence of Balmer line cores filled with emission in all observed phases (Figures 6 and 9), but additional time-domain observations and analysis is required to unambiguously determine the variability nature of WD J1653–1001. Out of the 28 DA(H)e stars, 57 per cent are photometrically variable and 29 per cent are spectroscopically variable. Note that these variability fractions are likely lower limits since not all DA(H)e have time-domain data.

It is clear that for WD J0412+7549 the photometric flux maximum corresponds to the minimum strength of emission lines, i.e. the photo-

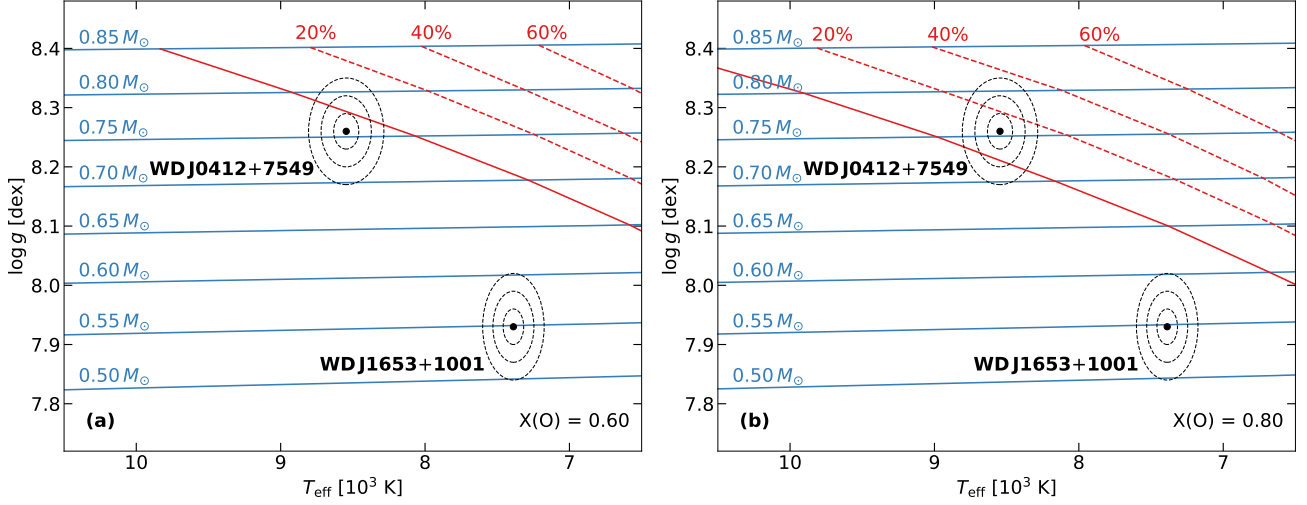


Figure 11. Evolutionary models showing the crystallized fraction (by mass) for WD J0412+7549 and WD J1653+1001 assuming core oxygen mass fractions of (a) 60 per cent and (b) 80 per cent. The photometric parameters of the two DAe stars are represented by black dots, with the dotted ellipses showing the 1σ , 2σ and 3σ uncertainties. Shown are the model sequences for white dwarf masses $0.50 - 0.85 M_{\odot}$ (blue tracks), the onset of crystallization (solid red line) and the evolutionary stages where the star is 20 per cent, 40 per cent or 60 per cent crystallized (dotted red lines).

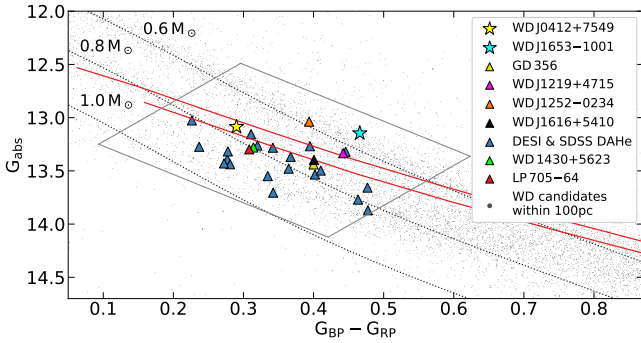


Figure 12. *Gaia* HRD zoomed-in on the white dwarf cooling sequence where DA(H)e reside, which is based off fig. 8 in Manser et al. (2023). The two DAe stars WD J0412+7549 and WD J1653+1001 (stars) are shown, in addition to the DAHe white dwarfs from the literature (triangles), compared to white dwarf candidates within 100 pc of the sun (grey dots; Gentile Fusillo et al. 2019). The grey box shows the region defined in Manser et al. (2023) which bounds the DA(H)e stars. The black dotted lines show the cooling tracks of $0.6 M_{\odot}$, $0.8 M_{\odot}$ and $1.0 M_{\odot}$ DA white dwarfs calculated with new model evolutionary sequences (discussed in Section 3.4) and a core oxygen mass fraction of 60 per cent. The red solid lines show the predicted onset of crystallization assuming core oxygen mass fractions of 60 per cent (lower) and 80 per cent (upper).

metric and spectroscopic variability are in anti-phase (Section 3.1.3) - which is the relationship predicted in Walters et al. (2021) for this star. The same phase relationship was found in the DAHe stars SDSS J125230.93-023417.72 (Reding et al. 2020), GD 356 (Walters et al. 2021), WD J1616+5410 (Manser et al. 2023), suspected in SDSS J121929.45+471522.8 (Gänsicke et al. 2020) and visually identified in LP 705-64 and WD J143019.29-562358.33 (Reding et al. 2023). Thus, the seven DA(H)e stars that have adequate phase coverage in spectroscopic observations and exhibit spectroscopic variability have a confirmed or suspected anti-phase relationship with photometric variability. An anti-phase relationship is indicative of a dark spot/region beneath an optically thin chromosphere,

whereas we would expect an in-phase relationship if there is a closely orbiting companion.

WD J0412+7549 has radial velocity variation of $\lesssim 40 \text{ km s}^{-1}$ and both DAe stars have no evidence of near-IR excess, suggesting that neither star has a stellar companion (see Section 4.2.1). This is consistent with the DA(H)e class in general, where none of the class members have confirmed stellar or planet mass companions.

4.2 What is causing the $H\alpha$ and $H\beta$ emission lines?

Both non-magnetic and magnetic mechanisms have been put forward as possible reasons for Balmer emission lines in cool white dwarfs ($T_{\text{eff}} \leq 8500 \text{ K}$). In the following subsections, we will discuss the feasibility of each of these mechanisms being present in the DAe stars WD J0412+7549 and WD J1653+1001.

4.2.1 Unseen companions

We now explore the possibility of a stellar or substellar companion, such as a brown dwarf or planet, orbiting the DAe stars and causing the Balmer emission lines. It is feasible that a white dwarf can have a planetary mass companion as it is well established that planets can survive the stellar evolution of their host star into a white dwarf (Villaver & Livio 2007; Mustill & Villaver 2012; Rao et al. 2018; Ronco et al. 2020). Recent observations have suggested planet candidates orbiting white dwarfs (Thorsett et al. 1993; Sigurdsson et al. 2003; Luhman et al. 2011; Gänsicke et al. 2019; Vanderburg et al. 2020; Blackman et al. 2021), but no substellar companions have been confirmed around DA(H)e stars at this time.

We are able to place upper mass limits on potential companions of WD J0412+7549 and WD J1653+1001 by comparing infrared photometry of these stars from 2MASS, JHK and WISE reported in the CatWISE2020 catalogue (Marocco et al. 2021) to brown dwarf flux models (Phillips et al. 2020). Despite neglecting background contaminated WISE photometry from all photometric fits performed in this work, we include it here as the peak wavelengths of late-spectral-type objects fall in the far-IR thus WISE measurements are optimal for placing limits on potential brown dwarf companions. The W1

band places the strongest constraints on companion spectral type due to a flux dip in brown dwarf models in *W2*. Using the M_{WD} we derived from photometry (Table 2) and the initial-to-final-mass relation (IFMR) from Cummings et al. (2018), we calculated the progenitor mass of WD J0412+7549 to be $3.1 \pm 0.2 M_{\odot}$ and the total age of the system to be 1.54 ± 0.13 Gyr. The photometry in the *W1* filter is 15.226 ± 0.023 mag which, with the total age of the system, places a mass constraint on a substellar companion no earlier than a T-type brown dwarf ($< 60 M_{\text{Jup}}$). Doing the same analysis for WD J1653–1001 reveals a progenitor mass of $0.8 - 0.9 M_{\odot}$ and the total age of the system to be > 10 Gyr. The *W1* measurement for this system is 14.347 ± 0.015 mag but there is no evidence that the white dwarf and close-proximity background main-sequence star have been resolved. Using the *W1* measurement and total age of the system, we can place a mass constraint of $< 80 M_{\text{Jup}}$ on a companion, which rules out a stellar companion and anything earlier than a brown dwarf. Even though the *W1* measurement is contaminated, we reach a similar result when using 2MASS photometry from the *JHK* filters.

If the Balmer line emission in these DAe stars originates from a companion, then we expect the orbital period to be the same as the photometric variability period. Kepler’s laws can be used to predict the radial velocity of the emission feature if it was emitted by a companion in WD J0412+7549. We do not entertain an inclination of 0° (face-on orbit) as we would not observe photometric variations in this case. Assuming an inclination of 90° (edge-on orbit), the companion would require a radial velocity variation with a lower limit of $\geq 400 \text{ km s}^{-1}$ compared to an observed radial velocity variation upper limit of $\approx 10 \text{ km s}^{-1}$ for WD J0412+7549. Even an inclination of 45° would require the companion to have a radial velocity of $\approx 280 \text{ km s}^{-1}$ which is still infeasibly large. Therefore, we can largely rule out that the emission is from a companion and instead it must originate from the stellar surface.

If DAe stars have a companion but the Balmer emission lines are assumed to originate from the white dwarf surface and the orbital period corresponds to the photometric period, then the radial velocity of the star will be dependent on the companion mass. During the companion’s orbit, the force exerted onto the star would cause the Balmer line emission cores and wings to radially shift with a consistent amplitude. With the current observations of WD J0412+7549, it is only possible to measure the radial velocity of the Balmer line emission cores but this is sufficient for our analysis. We can constrain a companion upper mass limit of $115 M_{\oplus}$ for a favourable edge-on inclination.

4.2.2 Magnetic mechanisms

It is possible that the same magnetic mechanism which causes the detectable magnetic field in DAHe stars is present in DAe stars and causes all objects in the DA(H)e class to have Balmer emission lines, yet the magnetic field in DAe stars is not strong enough to cause these lines to be Zeeman-split into triplets. Magnetic field lines could emerge for a certain T_{eff} and M_{WD} , resulting in an intrinsically-activated chromosphere for a limited amount of time, before the white dwarf continues to evolve along the cooling track as a DA or DAH. The undetectable magnetic field in DAe stars could therefore be due to them being at slightly different stages of the DA(H)e evolutionary phase which could cause the magnetic field to be smaller or buried below the photosphere as the field lines simply have not had time to emerge from the surface yet.

The origin of magnetic fields in isolated degenerate stars is not well understood, although several theories have been developed to explain

their presence, such as: fields remnant from the progenitor pre-main sequence (fossil fields) or main sequence stars that got trapped and retained in the non-convective core regions of the star and released upon the evolution into a white dwarf (Landstreet 1967; Angel et al. 1981; Braithwaite & Spruit 2004; Tout et al. 2004; Wickramasinghe & Ferrario 2005); a dynamo acting in the common envelope phase (Tout et al. 2004; Briggs et al. 2018; Belloni & Schreiber 2020) or during a merger (García-Berro et al. 2012); or a convective dynamo driven by white dwarf core crystallization (van Horn 1968; Isern et al. 2017; Schreiber et al. 2021a,b; Ginzburg et al. 2022).

The unipolar inductor model has been explored in the literature (Goldreich & Lynden-Bell 1969; Li et al. 1998; Wickramasinghe et al. 2010) as a potential mechanism for magnetism and the emission feature in DAHe stars (Gänsicke et al. 2020; Reding et al. 2020; Walters et al. 2021). This model involves the induction of an electric current from the close-in orbit of a rocky planet through the host star’s magnetosphere, which consequently heats up the host’s atmosphere at the magnetic poles causing emission. An in-phase relationship between photometric and spectroscopic variability is expected from the unipolar model. However, DA(H)e stars have been found to have an anti-phase relationship (Section 3.1.3), suggesting they host a photospheric dark spot below an optically thin emission region, i.e. with a temperature inversion above the photosphere, which is inconsistent with the unipolar model (Walters et al. 2021).

Observational evidence and the similar physical characteristics of DA(H)e stars suggest that the Balmer emission lines are caused by a mechanism internal to the white dwarf, such as magnetic emergence or an intrinsically-activated chromosphere. An active and hot chromosphere (above the photosphere) in polar magnetic regions would cause the change in intensity of Balmer emission lines which we observe as spectroscopic variability over the spin period, in addition to flux variations from underlying cooler/warmer photospheric regions which we observe as photometric variability as the white dwarf rotates. Note that photometric variability could also be caused by other magnetic effects (opacities, polarization) and more observations (e.g. multi-wavelengths) are needed to conclude whether the photometric temperature is variable over the surface (Fuller & Mathis 2023).

A local surface dynamo (or chromospheric activity itself) to explain magnetic field generation is ruled out as the amount of energy stored in the convection zone and upper layers is unable to explain magnetic fields larger than about 1 kG (Fontaine et al. 1973; Tremblay et al. 2015).

A crystallization-induced global dynamo has been theorized to cause the production and emergence of magnetic fields in isolated white dwarfs thus could be the reason for magnetism in DA(H)e stars (Isern et al. 2017; Schreiber et al. 2021a,b). The Balmer line emission could then result from the emergence at the stellar surface of these newly generated magnetic field lines. But, more recently, doubts have been raised on the efficiency of this mechanism due to the small convective velocities⁴ and kinetic energy flux reservoir (Fuentes et al. 2023). The onset of core crystallization depends on white dwarf mass and core chemical composition but otherwise occurs at a specific evolutionary stage, resulting in it being a possible explanation for the close clustering of DA(H)e stars on the *Gaia* HRD (Schreiber et al. 2021b).

Core crystallization combined with the white dwarf’s rotation has been predicted to sustain a global magnetic dynamo (Ginzburg et al. 2022). The dependence of these factors results in a relationship be-

⁴ This refers to slow compositionally-driven internal convection and it is unrelated to the surface dynamo discussed earlier.

tween the fraction of the core which is crystallized, the spin period and magnetic field strength (Schreiber et al. 2021a,b; Ginzburg et al. 2022; Fuentes et al. 2023). We used evolutionary model sequences to calculate the fraction of the DAe stars which is crystallized based on their photometric parameters (see Section 3.4). The core oxygen abundance in white dwarfs is poorly understood, thus uncertainty is introduced in our evolutionary model sequences as this parameter influences the onset of crystallization. To acknowledge this uncertainty, we calculated two sets of models: one with a standard core composition of 60 per cent oxygen (left panel of Figure 11); and one with a heavier core composition of 80 per cent oxygen (right panel of Figure 11). It is apparent that the onset of crystallization occurs earlier when a higher core oxygen abundance is assumed.

From our evolutionary model sequences, we cannot determine whether WD J0412+7549 has started to crystallize or not as it depends on its core composition (which is uncertain) and the precision of its T_{eff} and $\log g$ photometric parameters. If WD J0412+7549 has an 80 per cent core oxygen abundance, the crystallized fraction could be as high as 40 per cent at 3σ . We can exclude that WD J1653–1001 has started to crystallize considering up to 3σ of its photometric parameters and both 60 per cent and 80 per cent core oxygen abundances.

The position of DA(H)e stars on the *Gaia* HRD is compared to the onset of crystallization in Figure 12. In this work, we have improved the modelling in different ways and therefore we can now be relatively confident that the atmospheric parameters are robust. First, the photometric parameters ($T_{\text{eff}}/\log g$) of DA(H)e white dwarfs with 3D convective or 1D radiative models (accounting for magnetic effects) were shown to be similar (see Section 3.2). It has also recently been shown that photometric atmospheric parameters for cool ≈ 8000 K magnetic white dwarfs using non-magnetic models are likely to be accurate (McCleery et al. 2020; Hardy et al. 2023).

In addition, the crystallization sequences we used include up-to-date physics (see Section 3.4). When an oxygen mass fraction of 80 per cent is assumed, two out of 28 DA(H)e stars have not started to crystallize within 3σ . When an oxygen mass fraction of 60 per cent is assumed, out of the 28 DA(H)e white dwarfs seven have not started to crystallize within 1σ nor five within 3σ . Uncertainties still remain in crystallization models (e.g. Blouin et al. 2021), but at present the predicted onset of crystallization does not fully match with the emergence of DA(H)e stars, and even then it is expected that the emergence of surface magnetic fields from a crystallization dynamo will be delayed from the onset of crystallization (Ginzburg et al. 2022).

An anti-correlation between the magnetic field strength and the white dwarf spin period is expected for a crystallization-driven dynamo (Ginzburg et al. 2022). The tentative positive correlation found by Manser et al. (2023) in the nine DAHe stars with ZTF-determined spin periods and the three previously published DAHe stars is not in agreement with the relationship $B \propto P^{-1/2}$ found by Ginzburg et al. (2022) for a magnetic field generated by a crystallization-driven convective dynamo in single white dwarfs. This observation, coupled with the fact that some DAe stars have likely not started to crystallize, makes it challenging to unequivocally attribute crystallization as the universal origin mechanism for their magnetic fields. However, emergence of magnetic fields from another mechanism such as magnetic diffusion of pre-white dwarf fields over Gyr timescales, can still be an explanation for DA(H)e stars (Cantiello et al. 2016; Bagnulo & Landstreet 2021, 2022), even though it needs fine tuning for the emergence to almost coincide with the onset of crystallization.

From studies of volume limited samples, magnetism has been found to be rare and generally weak in young canonical mass

($\approx 0.6 M_{\odot}$) white dwarfs, yet the magnetic incidence appears to increase for cooling ages larger than 2 – 3 Gyr (Bagnulo & Landstreet 2022). This is likely evidence that magnetic fields emerge from the interior to the stellar surface within this age range. The delayed magnetic field emergence could explain the existence of DA(H)e stars and their close clustering on the *Gaia* HRD, rather than scenarios where the magnetic field has always been at the white dwarf surface. Field emergence is not unique to any magnetic generation scenario so we cannot narrow down the origin of the fields. It is yet to be determined whether DA(H)e stars were originally DA where a mechanism caused the emergence of both the magnetic field and spectral emission features together, or if they were DAH stars which were incident to a mechanism which produces Balmer line emission. However, the discovery of delayed magnetic field emergence – independent of DA(H)e observations – gives support to the scenario that DA are the progenitors of DA(H)e stars, suggesting Balmer line emission is connected to the magnetic field generation mechanism(s).

It is interesting to note that the DA(H)e variability strip in the *Gaia* HRD coincides with the maximum strength of the hydrogen opacity in the non-degenerate envelope (see fig. 6 of Saumon et al. 2022), and this opacity bump is even more sharply peaked in stellar radius for radiative magnetic structures (Tremblay et al. 2015). We speculate that it could result in instabilities and waves responsible for activity at the surface, but it would not explain a change in the incidence of magnetic white dwarfs with temperature (Bagnulo & Landstreet 2022).

4.3 An explanation for photometric variability in WD J0412+7549

In order to explain the causes of photometric variability, we used the *TESS* bandpass and integrated different white dwarf model fluxes to perform two tests. In the first test, we computed the flux using our best-fitting 3D convective DA model atmosphere without line emission, and then with added artificial line emission based on the observed Keck spectrum at peak emission. The flux variation was 0.04 per cent, which rules out that Balmer line emission is causing the observed photometric variation of $\approx 2.29 \pm 0.05$ per cent.

In the second test, we used our 1D radiative and 1D convective DA model atmospheres⁵ on opposing sides of the star to model convective and radiative magnetic regions, respectively (Figure 13). We assumed a constant effective temperature across the surface. The impact of magnetic fields on a stellar structure can be estimated from the plasma- β parameter ($\beta = 8\pi P/B^2$, where P is the thermal pressure and B the magnetic field strength). It was found from 3D magneto-hydrodynamic (MHD) simulations (Tremblay et al. 2015) that a value of $\beta \sim 1$ will inhibit convective energy transfer in the white dwarf atmosphere. Magnetic fields larger than this critical value, corresponding to 0.002 – 0.1 MG in DA white dwarfs (Cunningham et al. 2020), will therefore result in a largely radiative temperature stratification (Gentile Fusillo et al. 2018). For WD J0412+7549, the critical field to inhibit convection is $B \approx 0.01$ MG, so a plausible scenario to explain photometric variability is that one side of the star harbours a small magnetic field (above $B \approx 0.01$ MG but below the detection limit of 0.05 MG) resulting in a radiative structure, while other regions are able to remain convective (Tremblay et al. 2015, see also Section 3.2).

⁵ The use of 1D convective models is to allow for a better differential comparison using the same atmosphere code.

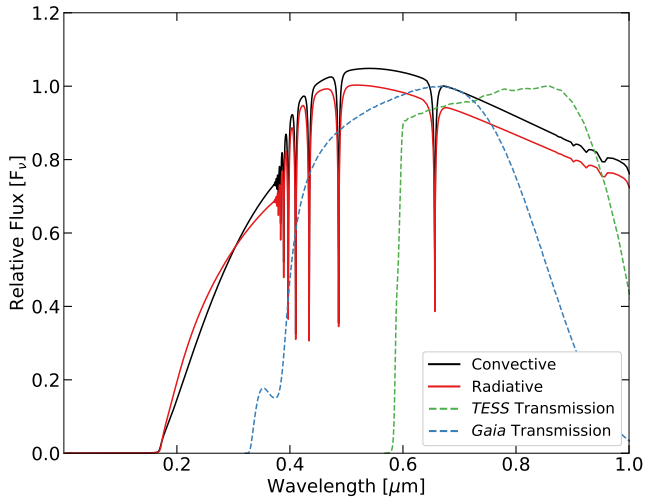


Figure 13. Model spectra created from the same 1D model atmosphere code with a pure-hydrogen equation-of-state, showing radiative (red curve) and convective ($ML2/\alpha = 0.8$; black curve) structures corresponding to opposing sides of the star. A constant effective temperature across the white dwarf surface is assumed. The normalized *TESS* (green) and *Gaia* (blue) bandpasses are shown.

The different atmospheric temperature stratifications in convective and magnetic regions result in different SEDs. We find that flux peaks on the convective side of the star in the *TESS* bandpass, with a flux deficit on the radiative side. A flux variation of ≈ 5 per cent is predicted between the two regions, which suggests that even subtle effects on the atmospheric structure from small magnetic fields ($\approx 10 - 50$ kG) could be responsible for the photometric *TESS* flux variation. Under this scenario, the photometric minimum corresponds to the radiative (magnetic) side, in line with the expectation of an active chromosphere and line emission in magnetic regions. While the effective temperature remains constant, the smaller flux in the *TESS* bandpass for the radiative region implies that light is emitted from a slightly cooler region of the atmosphere. This is analogous to the previously suggested scenario where DA(H)e stars have cool magnetic regions (Walters et al. 2021), but does not require a yet unexplained mechanism to change the effective temperature across the surface.

We note that the above prediction could be tested with multi-wavelength photometric studies and spectropolarimetry, to confirm that one or more phases have a radiative structure and magnetic field strength $\approx 10 - 50$ kG. We also note that this scenario is unlikely to apply for DAHe white dwarfs, in particular for GD 356 where spectropolarimetric observations suggest that in all rotation phases the surface is highly magnetic (Walters et al. 2021), hence likely radiative.

5 CONCLUSIONS

Two DAe white dwarfs, WD J0412+7549 and WD J1653–1001, have been discovered in the past three years. They have hydrogen-dominated atmospheres and exhibit $H\alpha$ and $H\beta$ line emission. These characteristics are the same as DAHe stars, yet DAHe stars have Zeeman-split Balmer emission lines indicating magnetism. The class DA(H)e incorporates DAe and DAHe stars due to the hypothesis that they have a similar origin, as their uncoincidental close clustering on

the *Gaia* HRD indicates these stars may be experiencing a short evolutionary phase where magnetic fields with vastly different strengths trigger Balmer line emission. The physical mechanism(s) causing DA(H)e stars is still unknown.

This work provides detailed follow-up of the two known DAe stars by presenting new time-domain spectroscopic observations and analysis of the latest photometric time-series data. Both DAe stars do not have detectable magnetic fields, with upper limits on magnetic field strength of $B < 0.05$ MG. We confirm that both DAe stars exhibit photometric and spectroscopic variability, which we interpret as the white dwarf spin period. WD J0412+7549 has a period of 2.2891144 ± 0.0000016 h and WD J1653–1001 has a tentative period of 80.534 ± 0.087 h. Additional photometric follow-up with larger phase coverage is needed to confidently determine the period of WD J1653–1001 as the current ZTF data is contaminated by an unresolved background main-sequence star.

WD J0412+7549 has spectroscopic data spanning its entire phase, including two high-resolution Keck spectra. We calculated the radial velocity of this star using its $H\alpha$ emission line and found an absence of significant radial velocity variation, which indicates it is originating from the white dwarf surface or chromosphere. The similar physical characteristics of DAe and DAHe stars (Section 4.1) suggests that the mechanism causing the Balmer line emission and photometric variability is in common, and likely intrinsic to the white dwarf, rather than a substellar companion body closely orbiting the stars (Walters et al. 2021). Furthermore, WD J0412+7549 has an anti-phase relationship between photometric (flux) and spectroscopic (emission) variability which is the same phase relationship found in DAHe stars. An anti-phase relationship is the expectation of a photospheric dark spot/region with a temperature-inverted and optically thin chromospheric emission region, and not of a closely orbiting companion.

We have shown that the photometric flux variation in WD J0412+7549 could be readily explained by radiative (magnetic) and convective hemispheres having different SEDs, with a threshold of $B \approx 10$ kG between the two faces. Testing this scenario would require better phase resolved limits on magnetic fields down to $1 - 10$ kG, a measurement that could be made difficult by the short rotation period.

It is possible that magnetic emergence has not occurred yet or has just started to occur in DAe stars, which explains their lack of a detectable magnetic field but similarities with DAHe stars. Therefore, the physical origin of their characteristics could be the same as DAHe stars. We explored magnetic mechanisms that could drive a magnetic field in isolated white dwarfs, including global and local surface dynamos. A global dynamo is created from the combination of core crystallization and the white dwarf rotation. Our modelling could not determine if WD J0412+7549 has started to crystallize but we conclude that WD J1653–1001 has not started to crystallize. Spectroscopic and multi-wavelength photometric follow-up of DAe stars is required to further understand their behaviours and to determine the origin of this class.

ACKNOWLEDGEMENTS

This project has received funding from the European Research Council under the European Union’s Horizon 2020 research and innovation programme (Grant agreement numbers 101002408 – MOS100PC and 101020057 – WDPLANETS) as well as the UK STFC consolidated grant ST/T000406/1. The authors acknowledge financial

support from Imperial College London through an Imperial College Research Fellowship grant awarded to CJM.

This work has made use of data from the European Space Agency (ESA) mission *Gaia* (<https://www.cosmos.esa.int/gaia>), processed by the *Gaia* Data Processing and Analysis Consortium (DPAC, <https://www.cosmos.esa.int/web/gaia/dpac/consortium>). Funding for the DPAC has been provided by national institutions, in particular the institutions participating in the *Gaia* Multilateral Agreement.

This paper includes data collected by the *TESS* mission. Funding for the *TESS* mission is provided by the NASA's Science Mission Directorate. This paper includes data collected by the *TESS* mission that are publicly available from the Mikulski Archive for Space Telescopes (MAST).

Based on observations obtained with the Samuel Oschin Telescope 48-inch and the 60-inch Telescope at the Palomar Observatory as part of the Zwicky Transient Facility project. ZTF is supported by the National Science Foundation under Grants No. AST-1440341 and AST-2034437 and a collaboration including current partners Caltech, IPAC, the Weizmann Institute for Science, the Oskar Klein Center at Stockholm University, the University of Maryland, Deutsches Elektronen-Synchrotron and Humboldt University, the TANGO Consortium of Taiwan, the University of Wisconsin at Milwaukee, Trinity College Dublin, Lawrence Livermore National Laboratories, IN2P3, University of Warwick, Ruhr University Bochum, Northwestern University and former partners the University of Washington, Los Alamos National Laboratories, and Lawrence Berkeley National Laboratories. Operations are conducted by COO, IPAC, and UW.

Some of the data presented in this work were obtained at the W. M. Keck Observatory, which is operated as a scientific partnership among the California Institute of Technology, the University of California and the National Aeronautics and Space Administration. The Observatory was made possible by the generous financial support of the W. M. Keck Foundation. We wish to recognize and acknowledge the very significant cultural role and reverence that the summit of Maunakea has always had within the indigenous Hawaiian community. We are most fortunate to have the opportunity to conduct observations from this mountain.

The William Herschel Telescope and Isaac Newton Telescope are operated on the island of La Palma by the Isaac Newton Group of Telescopes in the Spanish Observatorio del Roque de Los Muchachos of the Instituto de Astrofísica de Canarias.

Based on observations obtained at the international Gemini Observatory, a programme of NSF's NOIRLab, which is managed by the Association of Universities for Research in Astronomy (AURA) under a cooperative agreement with the National Science Foundation on behalf of the Gemini Observatory partnership: the National Science Foundation (United States), National Research Council (Canada), Agencia Nacional de Investigación y Desarrollo (Chile), Ministerio de Ciencia, Tecnología e Innovación (Argentina), Ministério da Ciência, Tecnologia, Inovações e Comunicações (Brazil), and Korea Astronomy and Space Science Institute (Republic of Korea).

Research at Lick Observatory is partially supported by a generous gift from Google. A major upgrade of the Kast spectrograph on the Shane 3 m telescope at Lick Observatory was made possible through generous gifts from William and Marina Kast as well as the Heising-Simons Foundation.

DATA AVAILABILITY

Spectroscopy from the WHT, Keck, INT, Gemini and Shane telescopes, in addition to photometry from ZTF, are available from their respective public archives. The *TESS* data are accessible via the MAST (Mikulski Archive for Space Telescopes) portal at <https://mast.stsci.edu/portal/Mashup/Clients/Mast/Portal.html>.

REFERENCES

- Angel J. R. P., Borra E. F., Landstreet J. D., 1981, *ApJS*, **45**, 457
- Astropy Collaboration et al., 2013, *A&A*, **558**, A33
- Astropy Collaboration et al., 2018, *AJ*, **156**, 123
- Astropy Collaboration et al., 2022, *ApJ*, **935**, 167
- Bagnulo S., Landstreet J. D., 2018, *A&A*, **618**, A113
- Bagnulo S., Landstreet J. D., 2021, *MNRAS*, **507**, 5902
- Bagnulo S., Landstreet J. D., 2022, *ApJ*, **935**, L12
- Bauer E. B., 2023, *ApJ*, **950**, 115
- Bauer E. B., Schwab J., Bildsten L., Cheng S., 2020, *ApJ*, **902**, 93
- Bédard A., Bergeron P., Fontaine G., 2017, *ApJ*, **848**, 11
- Bédard A., Bergeron P., Brassard P., Fontaine G., 2020, *ApJ*, **901**, 93
- Bédard A., Brassard P., Bergeron P., Blouin S., 2022, *ApJ*, **927**, 128
- Bellm E. C., et al., 2019, *PASP*, **131**, 018002
- Belloni D., Schreiber M. R., 2020, *MNRAS*, **492**, 1523
- Blackman J. W., et al., 2021, *Nature*, **598**, 272
- Blouin S., Daligault J., 2021, *Phys. Rev. E*, **103**, 043204
- Blouin S., Shaffer N. R., Saumon D., Starratt C. E., 2020, *ApJ*, **899**, 46
- Blouin S., Daligault J., Saumon D., 2021, *ApJ*, **911**, L5
- Braithwaite J., Spruit H. C., 2004, *Nature*, **431**, 819
- Briggs G. P., Ferrario L., Tout C. A., Wickramasinghe D. T., 2018, *MNRAS*, **478**, 899
- Brinkworth C. S., Burleigh M. R., Wynn G. A., Marsh T. R., 2004, *MNRAS*, **348**, L33
- Brinkworth C. S., Burleigh M. R., Lawrie K., Marsh T. R., Knigge C., 2013, *ApJ*, **773**, 47
- Cantiello M., Fuller J., Bildsten L., 2016, *ApJ*, **824**, 14
- Cassisi S., Potekhin A. Y., Pietrinferni A., Catelan M., Salaris M., 2007, *ApJ*, **661**, 1094
- Chambers K. C., et al., 2016, arXiv e-prints, p. [arXiv:1612.05560](https://arxiv.org/abs/1612.05560)
- Cummings J. D., Kalirai J. S., Tremblay P. E., Ramirez-Ruiz E., Choi J., 2018, *ApJ*, **866**, 21
- Cunningham T., Tremblay P.-E., Gentile Fusillo N. P., Hollands M., Cukanovaite E., 2020, *MNRAS*, **492**, 3540
- Cunningham T., et al., 2021, *MNRAS*, **503**, 1646
- Dálya G., et al., 2018, *MNRAS*, **479**, 2374
- De Gerónimo F. C., Battich T., Miller Bertolami M. M., Althaus L. G., Córscico A. H., 2019, *A&A*, **630**, A100
- Eyer L., et al., 2017, arXiv e-prints, p. [arXiv:1702.03295](https://arxiv.org/abs/1702.03295)
- Eyer L., et al., 2023, *A&A*, **674**, A13
- Ferrario L., de Martino D., Gänsicke B. T., 2015, *Space Sci. Rev.*, **191**, 111
- Ferrario L., Wickramasinghe D., Kawka A., 2020, *Advances in Space Research*, **66**, 1025
- Flewelling H. A., et al., 2020, *ApJS*, **251**, 7
- Fontaine G., Thomas J. H., van Horn H. M., 1973, *ApJ*, **184**, 911
- Fontaine G., Brassard P., Bergeron P., 2001, *PASP*, **113**, 409
- Fuentes J. R., Cumming A., Castro-Tapia M., Anders E. H., 2023, *ApJ*, **950**, 73
- Fuller J., Mathis S., 2023, *MNRAS*, **520**, 5573
- Gaia Collaboration et al., 2023, *A&A*, **674**, A34
- Gänsicke B. T., Schreiber M. R., Toloza O., Gentile Fusillo N. P., Koester D., Manser C. J., 2019, *Nature*, **576**, 61
- Gänsicke B. T., Rodríguez-Gil P., Gentile Fusillo N. P., Inight K., Schreiber M. R., Pala A. F., Tremblay P.-E., 2020, *MNRAS*, **499**, 2564
- García-Berro E., et al., 2012, *ApJ*, **749**, 25
- Gentile Fusillo N. P., Tremblay P. E., Jordan S., Gänsicke B. T., Kalirai J. S., Cummings J., 2018, *MNRAS*, **473**, 3693
- Gentile Fusillo N. P., et al., 2019, *MNRAS*, **482**, 4570

- Giammichele N., et al., 2018, *Nature*, **554**, 73
- Giammichele N., Charpinet S., Brassard P., 2022, *Frontiers in Astronomy and Space Sciences*, **9**, 879045
- Gianninas A., Bergeron P., Ruiz M. T., 2011, *ApJ*, **743**, 138
- Ginzburg S., Fuller J., Kawka A., Caiazzo I., 2022, *MNRAS*, **514**, 4111
- Goldreich P., Lynden-Bell D., 1969, *ApJ*, **156**, 59
- Greenstein J. L., McCarthy J. K., 1985, *ApJ*, **289**, 732
- Guidry J. A., et al., 2021, *ApJ*, **912**, 125
- Hardy F., Dufour P., Jordan S., 2023, *MNRAS*, **520**, 6111
- Hook I. M., Jørgensen I., Allington-Smith J. R., Davies R. L., Metcalfe N., Murowinski R. G., Crampton D., 2004, *PASP*, **116**, 425
- Isern J., García-Berro E., Külebi B., Lorén-Aguilar P., 2017, *ApJ*, **836**, L28
- Jura M., 2003, *ApJ*, **584**, L91
- Koester D., Provençal J., Shipman H. L., 1997, *A&A*, **320**, L57
- Landstreet J. D., 1967, *Physical Review*, **153**, 1372
- Landstreet J. D., 1987, *MNRAS*, **225**, 437
- Li J., Ferrario L., Wickramasinghe D., 1998, *ApJ*, **503**, L151
- Lomb N. R., 1976, *Ap&SS*, **39**, 447
- Luhman K. L., Burgasser A. J., Bochanski J. J., 2011, *ApJ*, **730**, L9
- Manser C. J., et al., 2023, *MNRAS*, **521**, 4976
- Marocco F., et al., 2021, *ApJS*, **253**, 8
- Masci F. J., et al., 2019, *PASP*, **131**, 018003
- McCleery J., et al., 2020, *MNRAS*, **499**, 1890
- Munday J., et al., 2023, *MNRAS*, **518**, 5123
- Mustill A. J., Villaver E., 2012, *ApJ*, **761**, 121
- O'Brien M. W., et al., 2023, *MNRAS*, **518**, 3055
- Paturel G., Petit C., Prugniel P., Theureau G., Rousseau J., Brouty M., Dubois P., Cambrésy L., 2003, *A&A*, **412**, 45
- Pedregosa F., et al., 2011, *Journal of Machine Learning Research*, **12**, 2825
- Phillips M. W., et al., 2020, *A&A*, **637**, A38
- Rao S., Meynet G., Eggenberger P., Haemmerlé L., Privitera G., Georgy C., Ekström S., Mordasini C., 2018, *A&A*, **618**, A18
- Reding J. S., Hermes J. J., Vanderbosch Z., Dennihy E., Kaiser B. C., Mace C. B., Dunlap B. H., Clemens J. C., 2020, *ApJ*, **894**, 19
- Reding J. S., Hermes J. J., Clemens J. C., Hegedus R. J., Kaiser B. C., 2023, *MNRAS*, **522**, 693
- Renedo I., Althaus L. G., Miller Bertolami M. M., Romero A. D., Córscico A. H., Rohrmann R. D., García-Berro E., 2010, *ApJ*, **717**, 183
- Ricker G. R., et al., 2014, in Oschmann Jacobus M. J., Clampin M., Fazio G. G., MacEwen H. A., eds, *Society of Photo-Optical Instrumentation Engineers (SPIE) Conference Series Vol. 9143*, *Space Telescopes and Instrumentation 2014: Optical, Infrared, and Millimeter Wave*. p. 914320 ([arXiv:1406.0151](https://arxiv.org/abs/1406.0151)), doi:10.1117/12.2063489
- Ronco M. P., Schreiber M. R., Giuppone C. A., Veras D., Cuadra J., Guilera O. M., 2020, *ApJ*, **898**, L23
- Salaris M., Cassisi S., Pietrinferni A., Kowalski P. M., Isern J., 2010, *ApJ*, **716**, 1241
- Salaris M., Cassisi S., Pietrinferni A., Hidalgo S., 2022, *MNRAS*, **509**, 5197
- Saumon D., Blouin S., Tremblay P.-E., 2022, *Phys. Rep.*, **988**, 1
- Scargle J. D., 1982, *ApJ*, **263**, 835
- Scharwächter J., et al., 2018, in Evans C. J., Simard L., Takami H., eds, *Society of Photo-Optical Instrumentation Engineers (SPIE) Conference Series Vol. 10702*, *Ground-based and Airborne Instrumentation for Astronomy VII*. p. 107022T, doi:10.1117/12.2313058
- Schreiber M. R., Belloni D., Gänsicke B. T., Parsons S. G., Zorotovic M., 2021a, *Nature Astronomy*, **5**, 648
- Schreiber M. R., Belloni D., Gänsicke B. T., Parsons S. G., 2021b, *MNRAS*, **506**, L29
- Sigurdsson S., Richer H. B., Hansen B. M., Stairs I. H., Thorsett S. E., 2003, *Science*, **301**, 193
- Silvestri N. M., et al., 2006, *AJ*, **131**, 1674
- Silvestri N. M., et al., 2007, *AJ*, **134**, 741
- Skrutskie M. F., et al., 2006, *AJ*, **131**, 1163
- Smith J. C., et al., 2012, *PASP*, **124**, 1000
- Straniero O., Domínguez I., Imbriani G., Piersanti L., 2003, *ApJ*, **583**, 878
- Stumpe M. C., et al., 2012, *PASP*, **124**, 985
- Thorsett S. E., Arzoumanian Z., Taylor J. H., 1993, *ApJ*, **412**, L33
- Tout C. A., Wickramasinghe D. T., Ferrario L., 2004, *MNRAS*, **355**, L13
- Tremblay P. E., Ludwig H. G., Steffen M., Freytag B., 2013, *A&A*, **559**, A104
- Tremblay P. E., Fontaine G., Freytag B., Steiner O., Ludwig H. G., Steffen M., Wedemeyer S., Brassard P., 2015, *ApJ*, **812**, 19
- Tremblay P. E., et al., 2020, *MNRAS*, **497**, 130
- Vanderburg A., et al., 2020, *Nature*, **585**, 363
- Venner A., Blouin S., Bédard A., Vanderburg A., 2023, *MNRAS*, **523**, 4624
- Villaver E., Livio M., 2007, *ApJ*, **661**, 1192
- Vogt S. S., et al., 1994, in Crawford D. L., Craine E. R., eds, *Society of Photo-Optical Instrumentation Engineers (SPIE) Conference Series Vol. 2198*, *Instrumentation in Astronomy VIII*. p. 362, doi:10.1117/12.176725
- Walters N., et al., 2021, *MNRAS*, **503**, 3743
- Wickramasinghe D. T., Ferrario L., 2005, *MNRAS*, **356**, 1576
- Wickramasinghe D. T., Farihi J., Tout C. A., Ferrario L., Stancliffe R. J., 2010, *MNRAS*, **404**, 1984
- Wright E. L., et al., 2010, *AJ*, **140**, 1868
- van Horn H. M., 1968, *ApJ*, **151**, 227

APPENDIX A: TIME-DOMAIN SPECTRA OF WD J0412+7549

This paper has been typeset from a $\text{\TeX}/\text{\LaTeX}$ file prepared by the author.

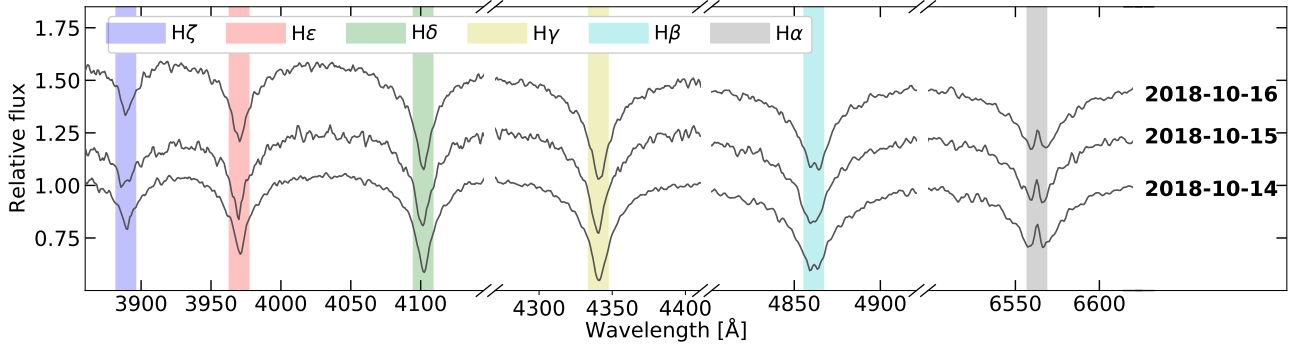


Figure A1. WHT spectra from three consecutive nights of observations of WDJ0412+7549, taken around the H α to H ζ line regions. Three exposures were taken on 2018 October 14 however we show the stacked spectrum here. The observation UT dates are shown on the right of the plot. Spectra are convolved with a Gaussian with a FWHM of 2 Å and offset vertically for clarity.

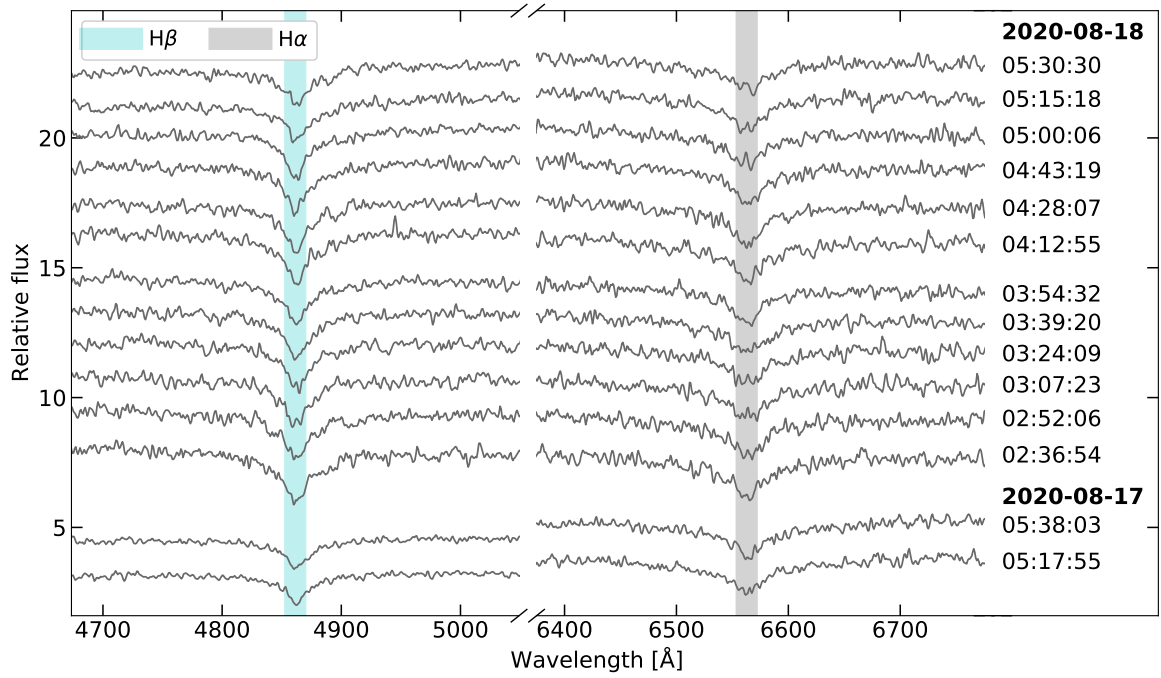


Figure A2. 14 exposures of INT IDS spectroscopy taken around the emission core of H α and H β . The observation UT date and start times are shown on the right of the plot. Spectra are convolved with a Gaussian with a FWHM of 2 Å and offset vertically for clarity.

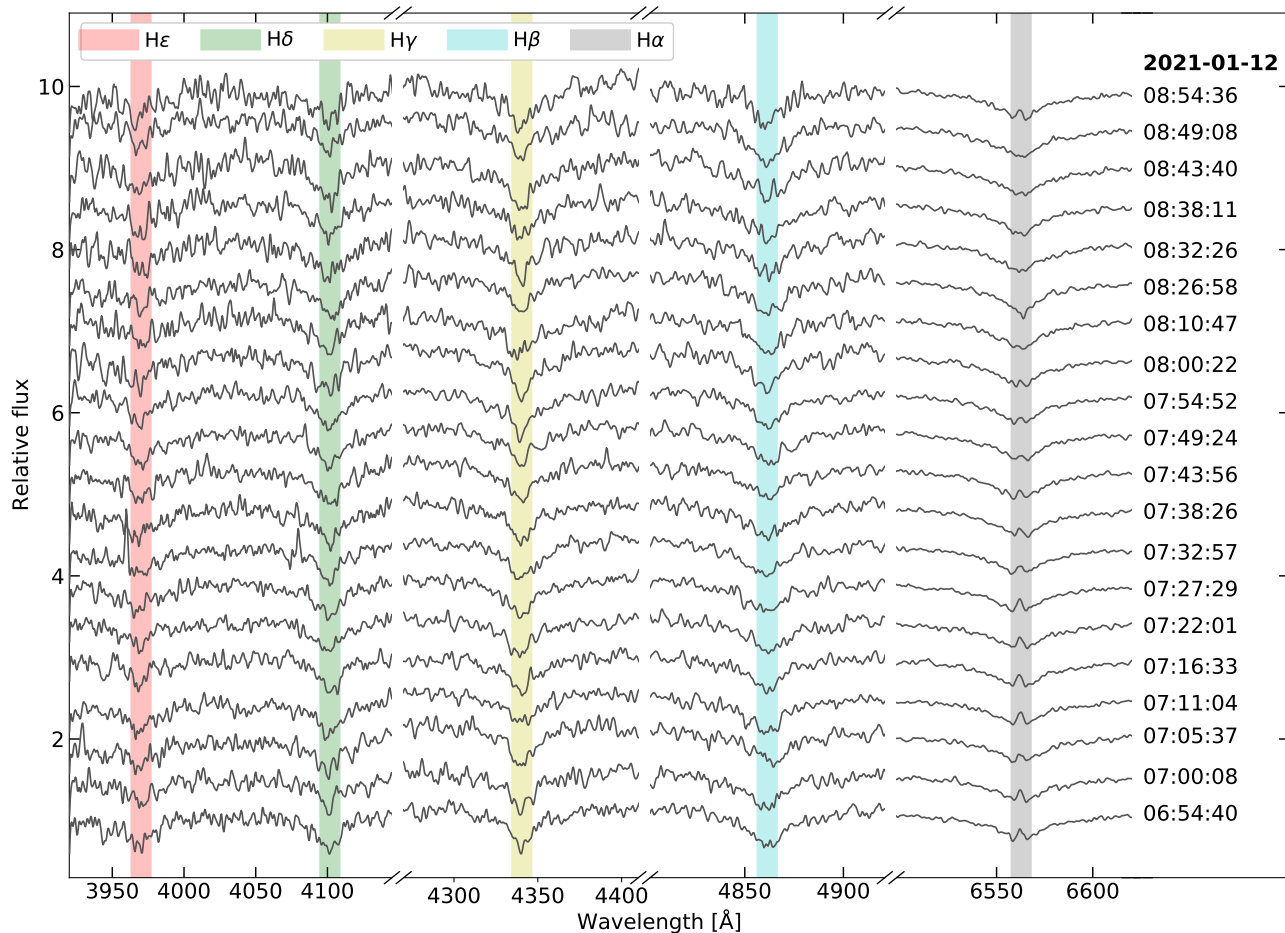


Figure A3. Gemini spectra of the 20 exposures taken on 2021 January 12 of WD J0412+7549 around the H α to H δ line regions. The observation UT date and start times are shown on the right of the plot. Spectra are convolved with a Gaussian with a FWHM of 3 Å and offset vertically for clarity.